TÉCNICO LISBOA

Performance Analysis of a Cryogenic Induction Machine

Luís Fernando Dias Bucho

Thesis to obtain the Master of Science Degree in

Electrical and Computer Engineering

Supervisor(s): Prof. Dr. João Filipe Pereira Fernandes
Prof. Dr. Andrea Cavagnino

Examination Committee

Chairperson: Prof. Dr. Célia Maria Santos Cardoso de Jesus
Supervisor: Prof. Dr. João Filipe Pereira Fernandes
Member of the Committee: Prof. Dr. Luís Guilherme Barbosa Rolim

November 2021

Declaration

I declare that this document is an original work of my own authorship and that it fullfils all the requirements of the Code of Conduct and Good Practices of the Universidade de Lisboa.

Dedicated to Maria Lourdes Barriguinha Granadeiro

Acknowledgments

To Prof. João Fernandes, thank you for the trust in me, help, guidance, extreme kindness and the incredible work you do with so much passion. I feel privileged for this opportunity and i am eternally grateful for it.

To Prof. Cavagnino, Prof. Silvio and Marco, thank you for your help, guidance, your questions and interest. For this i feel tremendously privileged and honoured.

To Prof. Paulo Branco, Pedro, Gui, Franscisco and Sr. Duarte, i will never forget your kindness. Thank you for sharing your thoughts and expertise with me, for all the jokes and coffee breaks.

To Prof. Pedro Abreu, thank you for inspiring me and being there for me when i most needed.

To my father, my hero, thank you for being who you are, you have no idea how proud i am for being your son. My mother and sister, my warriors, thank you for your relentless sacrifice and unmatched strength. I am extremely proud of you.

To my friends and extended family, couldn't have done it without you, my sincere thank you. Pedro Guilherme, a special thanks to you for the trust and for changing my life.

My star in the cosmos, Prof. Lourdes, this one is for you.

Resumo

Atualmente, o desenvolvimento de topologias de máquinas elétricas de elevada densidade de potência tem vindo a ser tópico de investigação devido aos objectivos mundiais para a eletrificação da mobilidade e a nova geração de sistemas industriais. Estudos recentes têm apontado o uso de máquinas de indução criogénicas como uma solução fiável, eficiente e de baixo custo, capaz de superar o desempenho das máquinas síncronas e de relutância mais avançadas.

Nesta tese, é analisado o desempenho de uma máquina de indução convencional de 90W, submersa em azoto líquido. A influência significativa da temperatura e do efeito pelicular, tanto nos parâmetros do circuito equivalente, como no desempenho geral da máquina é estudada recorrendo a métodos analíticos e validada em testes experimentais. Para validar os resultados analíticos obtidos, desenvolveram-se procedimentos e montagens experimentais, onde o motor de 90W é submergido e testado em azoto líquido.

As conclusões presentes nesta tese, demonstram que é possível obter melhorias significativas nas densidades de binário e potência, quando uma máquina de indução é operada em temperaturas muito baixas. Estes resultados são de especial interesse para as indústrias aeronáutica e aeroespacial, onde a massa dos sistemas de propulsão é de extrema importância. Estas indústrias têm feito, recentemente, um grande esforço na eletrificação dos seus sistemas propulsores, e estão a considerar, atualmente, a aplicação de motores de indução criogénicos como uma alternativa mais fiável e simples aos motores supercondutores que ainda não atingiram a sua maturidade.

Os resultados obtidos mostram um aumento de 21.3% na eficiência do motor, passando de 63.9% para 85.2%. Este aumento considerável na eficiência leva a um aumento de 170.8% de binário e um aumento de 188.5% de potencia mecânica, no ponto de eficiência máxima.

Palavras-chave: Maquinas Electricas, Motor de Indução Criogénico, Circuito Equivalente de Steinmetz, Desempenho Electro-Mecânico, Azoto Líquido, Arrefecimento Criogénico

Abstract

Recent research, in the field of electric machines, has been focused on developing high power density designs to be used in new generation industrial and drive systems applications. These new developments have suggested the use of cryogenic induction motors as a reliable, efficient and low cost solution, capable of outperforming the most advanced synchronous and reluctance motors.

In this thesis the performance of a conventional 90W induction motor submerged in liquid nitrogen is analysed. The significant influence of both temperature and skin effect in the equivalent circuit parameters and the overall performance of the machine is analytically studied and experimentally proven. To validate the obtained analytical results, experimental procedures and experimental setups were developed using the induction machine submerged in liquid nitrogen.

The findings achieved in this work show that considerable improvements in torque and power densities can be made when operating an induction motor in very low temperatures. They are of particular interest to aircraft and aerospace applications where weight is of the most importance. These applications have focused their recent efforts in the electrification of their propulsion systems, and are now considering cryogenic induction motors as a more reliable and simple alternative to superconducting machines which have still high costs and are not yet a mature solution.

The results show a 21.3% increase in motor efficiency, from 63.9% to 85.2%. This significant increase in efficiency, results in a 170.8% increase in torque and a 188.5% increase in mechanical output power at peak efficiency.

Keywords: Electrical Machines, Cryogenic Induction Motor, Steinmetz Equivalent Circuit, Electromechanical Performance, Liquid Nitrogen, Cryogenic Cooling

Contents

List of Tables

List of Figures

Nomenclature

A	Cross section area
A_{bar}	Cross sectional area of rotor bar
I_a	DC generator's armature current
I_a	DC generator's field current
I_b	Total current in rotor slot
I'_r	Rotor current refered to stator
I_s	Magnetizing current
I_s	Stator current
I_{load}	Load current
I_{pDC}	Uniformly distributed DC current in the p^{th} rotor slot layer
K_L	Skin effect inductance correction coefficient
K_R	Skin effect resistance correction coefficient
L_p	Inductance of the p^{th} rotor slot layer
L_{AC}	Conductor AC inductance
L_{DC}	Conductor DC inductance
N_r	Rotor angular velocity in revolutions per minute
P_e	Eddy current power loss
P_h	Hysteresis power loss
P_{AC}	Total AC losses in rotor bar
P_{DC}	Total DC losses in rotor bar
P_{active}	Phase active power magnitude
$P_{blockedrotor}$	Blocked rotor test active power magnitude

P_{cu} Copper power loss magnitude

P_{fe} Iron power loss

P_{mec} Mechanical power loss magnitude

P_{noload} No-Load active power magnitude

$Q_{blockedrotor}$ Blocked rotor test reactive power magnitude

Q_{noload} No-Load reactive power magnitude

R Resistance

R^2 Coefficient of determination

R_p Resistance of the p^{th} rotor slot layer

R'_r Rotor resistance referred to stator

R_s Stator resistance

R_{AC} Conductor AC resistance

R_{DC} Conductor DC resistance

R_{fe} Equivalent iron losses resistance

$R_{smeasured}$ Measured stator winding resistance

T Temperature

T_0 Reference temperature

U_a DC generator's armature voltage

U_s Stator voltage

U_{load} Voltage at load terminals

U_m Magnetizing voltage

W_{mAC} AC magnetic energy in rotor slot

W_{mDC} DC magnetic energy in rotor slot

X'_{lr} Rotor leakage reactance refered to stator

X_{ls} Stator leakage reactance

X_m Magnetizing reactance

$\Delta\bar{\phi}_p$ Magnetic leakage flux between the p^{th} and $(p+1)^{th}$ rotor slot layer

α_{cu} Copper temperature coefficient

$\bar{I}_1$	Estimation of initial current in bottom layer of rotor slot
$\bar{I}_p$	Current of the p^{th} rotor slot layer
$\boldsymbol{B}$	Magnetic flux density
$\boldsymbol{B}_p$	Magnetic flux density of the p^{th} rotor slot layer
δ	Skin depth
ϵ	Electric permittivity of conductor
η	Efficiency
μ	Magnetic permeability of conductor
μ_0	Magnetic permeability of vacuum
μ_r	Relative magnetic permeability of conductor
ω	Angular frequency of currents
ρ	Resistivity at given temperature
ρ_0	Resistivity at reference temperature
ρ_{Al}	Aluminium resisitivity
ρ_{FeSi}	Silicon iron resisitivity
ρ_{Fe}	Iron resisitivity
ρ_{cu}	Copper resisitivity
σ_{Al}	Aluminium electric conductivity
b_p	Width of the p^{th} rotor slot layer
e	Euler's number
f	Frequency of electric current
f_r	Frequency of rotor current
f_s	Frequency of stator current
h_p	Height of the p^{th} rotor slot layer
h_t	Total height of rotor slot
l	Length of conductor
l_{stack}	Rotor slot length
n	Number of rotor bar layers in multilayer approach method
s	Slip

Glossary

ARPA	Advanced Research Projects Agency
CERN	Conseil Européen pour la Recherche Nucléaire
EU	European Union
FeSi	Silicon Iron alloy
HTS	High-temperature superconductivity
IM	Induction machine
LH2	Liquid hydrogen
LN2	Liquid nitrogen
LNG	Liquefied natural gas
NEMA	National Electrical Manufacturers Association
PET	Polyethylene terephthalate
PMSM	Permanent magnet synchronous motor
PM	Permanent magnets
RMS	Root mean square

Chapter 1

Introduction

This first chapter aims at guiding the readers through this thesis. Here, the relevant milestones and problems that led to this thesis subject of study are described. Additionally, the objectives of this thesis are clearly stated and described. Also, an outline of this document is presented as well as a summary of each chapter content.

1.1 Motivation

The strive for maximum efficiency and maximum specific power in electric machines have been one of the main focus of the academy and industry since the first commercial electric motors were developed by Ferraris [1] , Tesla [2] and Dolivo-Dobrovolsky [3] in the late 1880's, early 1890's. Since then, a number of improvements and different typologies were introduced to achieve the final goal of a reliable, more efficient, low cost and easy to control electric motor. Today's power grid loads are dominated by the induction motor as it proved to be the most versatile, reliable and low cost design. Around 50% of energy consumed today is used by electric drives, where 40% is due to electric machines alone [4]. From these 40%, induction motors account for 96% of energy consumed [5]. It is clear that any efficiency improvement in this sector can have a very significant impact on, not only, energy savings, but also on cost savings due to the sheer amount of induction machines used as mechanical power sources and asynchronous generators. Both NEMA and the EU have, in the past 20 years put forward regulation, raising the efficiency requirements for new electric motors production [6]. This effort has had the intended result of increasing efficiency related research and create new, more efficient, manufacturing processes. From the point of view of the induction motor, although these regulations and research have increased the efficiency of machines, it also highlighted some limitations present in this solid yet old design. The induction motor is intrinsically less efficient than synchronous or reluctance motors due to the nature of the induction phenomena. We have reach a point where improvements in the induction motor efficiency must include new and more expensive magnetic and electric materials meaning that the cost of manufacturing must increase as well, therefore, the arguments that the induction machine is a very simple and easy to manufacture design seems to be at risk. One, hope inducing,

improvement was the discovery of high temperature superconductivity in 1986 [7] that led a number of engineers and scientists to research a superconducting version of the induction machine, in a bid to maximize efficiency. This journey proved to be a complex one, with material science and manufacturing as the bottleneck. One overlooked step in the superconducting electric machine research process was the required cryogenic cooling. Indeed this part of the process is regularly seen as a requirement for superconducting machines and despite the substantial attention given to it, it still is a major barrier.

In the past, cryogenic cooling was something reserved for a few areas of interest in science, mainly in chemistry and physics research. This was true until the second world war. In the mid 1950's the technological race created a space where applied cryogenics would flourish, specially in manufacturing industry and military applications. Today a few important applications, granted in very niche segments of industry and science, of cryogenic induction motors must be noted. In the aerospace industry these cryogenic motors are commonly used as pumps to auxiliary fuel or cooling systems, mainly using liquid hydrogen [8] working at a temperature of -253ºC. These cryogenic pumps are also used in advanced experimental physics research as in CERN [9] and Nuclear research [10]. Furthermore, military applications such as ship and plane propulsion are also studied and implemented, coupled with superconducting machines [11]. The most common application in industry though is in the energy sector, cryogenic induction motors working as pumps in liquid gas transportation [12].

This increase in cryogenic motors use stems from the increasing use and accessibility of cryogenic fluids in industrial and commercial applications, most notably liquid nitrogen, which is an easy, cheap fluid to produce, very stable and nonreactive. All of these new improvements and applications allow one to think of cryogenic induction motors not as solely a requirement to superconducting machines but also an opportunity to improve efficiency of the current machines, either by especially designing cryogenic induction motors or even converting the existing convectional ones into cryogenic machines, with the appropriate modifications to ensure material stability under cryogenic environment, thereby improving significantly the efficiency and power density of these types of motors.

1.2 Objectives

The main objective of this thesis is to analyse the performance of a conventional induction motor in cryogenic conditions. For this, the induction motor performance as a conventional ambient temperature motor is analysed, to be used as a baseline for comparison. The single-phase steady-state equivalent circuit is used for the analysis using experimental tests to compute the equivalent circuit parameters, both for ambient and cryogenic conditions. With these parameters, simulations are computed to use as reference and explore the influence that the cryogenic temperature has both on the physical electromagnetic phenomena that are present in the induction motor and on the equivalent circuit parameters themselves. Furthermore, experimental tests are going to be made to validate the simulations, and the methods, usually used in conventional machines but applied this time in the cryogenic regime. Also the methods and solutions used in this thesis are ultimately intended to serve as a guide to future experiments in cryogenic induction motors and cryogenic electric machines in general, including the

conversion of existing conventionally designed motors into cryogenic ones.

1.3 Thesis Outline

This thesis is divided into six chapters, starting with some background information about cryogenic motors and ending up by summarizing the findings and methods used in the experimental study. Below follows a description of the contents of each chapter.

- Chapter 2 - Background - In this chapter a brief history of cryogenic induction machines is presented. Their applications in the past and present, as well as possible future ones. Also, the historic advantages and disadvantages of this type of electric machine are explored. Finally the use of cryogenic induction machines outside of the superconducting machines sphere of influence is analysed.

- Chapter 3 - Electromechanical Performance of Cryogenic Induction Machines - This chapter explores the effects of cryogenic temperatures in the electrical and magnetic properties of the induction motor materials. The non linear resistivity characteristics of copper and aluminium under very low temperatures are shown and analysed. The influence of temperature and skin effect in the equivalent circuit parameters is detailed. Also torque, efficiency and mechanical power numerical simulations for the induction machine to be tested are computed, and the results explored.

- Chapter 4 - Experimental Setups and Methodology - In this chapter the experimental setups used in the tests are shown and explained as well as measuring setups. Preparation and testing of the machine bearings is shown and the methods explained. Finally, the methods used for the motor equivalent circuit parameters experimental determination are detailed.

- Chapter 5 - Results - Here the experimental results for ambient and cryogenic temperature tests are shown. Torque and efficiency curves obtained experimentally are compared with the simulated results and the methods validated. Moreover, 1h stability load tests are shown and discussed. Finally, measured losses in the machine are shown and compared for both regimes of operation.

- Chapter 6 - Conclusions - This last chapter summarizes the findings and achievements in this thesis. Also, future work and investigations are proposed as necessary steps to reach a final and solid understanding of the physical phenomena that dominates in the cryogenic regime for electric machines.

Chapter 2

Background

2.1 Early Applications of Cryogenic Electric Machines

The use of cryogenic induction motors goes back to the early second half of the 20^{th} century. The first application of a cryogenic induction motor was in the Liquefied Natural Gas (LNG) energy sector, where they were used as pumps to transport LNG at -164ºC from refining plants to LNG container ships and from ship to consumers shore storage facilities [13, 14]. This first generation of cryogenic induction motor pumps were introduced to replace traditional hydraulic-Internal combustion engines and non-submerged hydraulic-electric pump systems. These non-submerged pump systems required complex rotating seals in the motor shaft interfaces which were prone to failure [14]. Additionally pumping systems at that time required at least 2 different motor pumps, one for high pressure transport (Plant to Ship) and low pressure pumps (Ship to Truck/storage), these different pumps would be at different heights and distances from the source of fluid leading to complex hydraulic problems arising. The use of simple variable frequency control methods allowed the use of just one pump that would do both high pressure and low pressure pumping. Prior to the 1950's not much research was conducted in cryogenic induction motor, in fact, this first generation cryogenic submerged pumps used conventionally designed air-cooled induction motors used by a variety of industries at the time. The introduction of these cryogenic induction motor pumps were therefore a result of a serious effort into simplifying these cryogenic pumping systems and making them more reliable. Figure 2.1 shows a size comparison of a air-cooled and cryo-cooled generator/motor pump unit.

By the end of the 1950's considerable empirical research had been made on induction motor applications for cryogenic pump systems and major advantages over previous systems and air-cooled induction motors identified. The space race of the 1960's saw a new application of cryogenic induction machine pumps in the form of liquid hydrogen (-253ºC), oxygen (-183ºC) pumps for missiles and rockets [15]. At this stage a wide range of cryogenic induction motors were tested, from small 147W up to 37kW. The significant decrease of joule losses was identified as the main driver for this research, specially for the case of hydrogen, were the resistivity of copper is 1.4% of that at 20ºC [15]. This allowed for an increase in motor torque densities, vital for space applications. Furthermore, Joule losses were used to increase

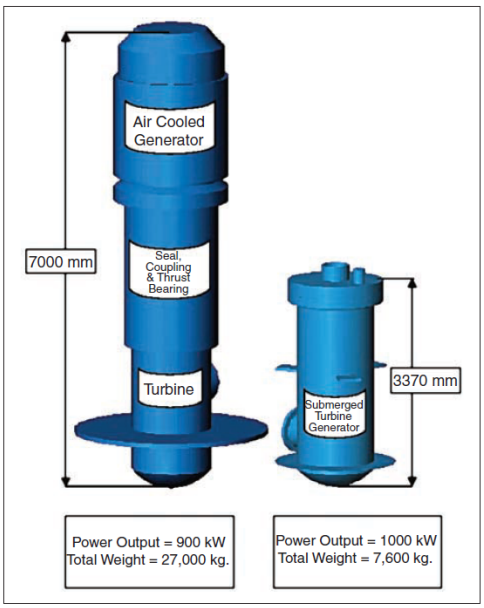

Figure 2.1: Size comparison between 900 kW air-cooled generator plus accessories and 1000 kW submerged generator of the same speed and voltage[13]

the overall efficiency of the missile's propulsion systems, by using this heat to heat the hydrogen fuel prior to vaporization.

A comparative study was made using a small conventional air-cooled 1.54kW three phase induction motor [15]. The performance of the motor in ambient temperature was compared to its performance in liquid hydrogen. Also, a cryogenic design version of the same motor was built and compared with the conventional one, this cryogenic motor was designed to have the same ratings in LH2 as the air-cooled motor in ambient temperature. The results of these tests are shown in figure 2.2

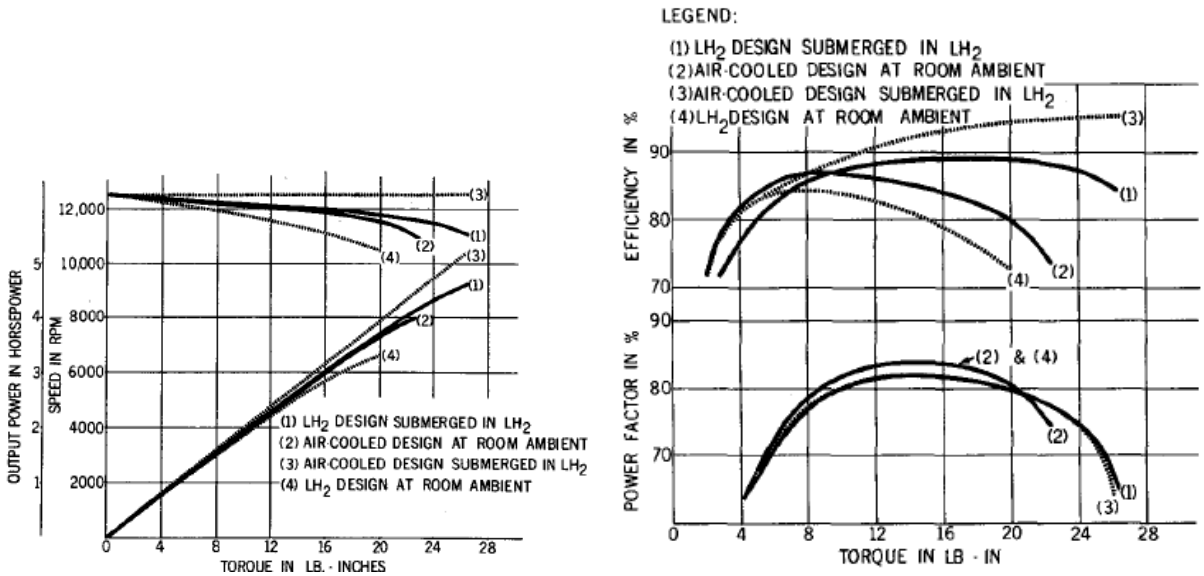

(a)Output power Air-cooled vs LH2 motors (b)PF and efficiency Air-cooled vs LH2 motors

Figure 2.2: Air-Cooled IM and LH2 designed IM comparison [15]

From these results it was apparent that a cryogenic designed motor was superior to an air-cooled motor with the same ratings. In low load condition, where iron and mechanical losses are dominant, both machines resulted in similar performance. For high load though, copper losses dominate and the LH2 designed motor showed a significant improvement in efficiency. At a load torque of 2.42Nm, twice the rated load of the air-cooled IM, the LH2 designed motor achieved a stable efficiency of 88% while the air-cooled motor achieved close to 79% efficiency.

It is important here to say that the air-cooled motor had a maximum thermally stable output power of 1.54kW while the LH2 motor could operate continuously at 3kW before entering the unstable zone (pull out torque). Furthermore the 1.54kW continuous operation of the air-cooled IM was only possible in low altitude applications, since its intended application in high altitude and space environment would come with a severe de-rating, due to cooling constraints.

The performance of the air-cooled motor submerged in liquid hydrogen (curve 3) also showed important results, outperforming the formally discussed designs due to the lower copper losses of the conductors (LH2 motor was designed to have the same resistance in -253ºC as the air-cooled motor in 20ºC). Despite this the air-cooled motor submerged in hydrogen was considered impractical due to its 0.02Nm staring torque compared to 1.67Nm in the LH2 designed motor. Some issues and possible improvements were also identified at this stage. The problem of low starting torque due to low rotor resistance in the air-cooled submerged test should be addressed by using an alloy instead of pure metal conductors, this would allow a compromise between a cryogenic designed motor with a high power density and the high efficient conventionally designed motor submerged in hydrogen. In addition an increase of 25% in iron losses in cryogenic temperatures was identified, highlighting the need for further iron losses research. Finally conductor dielectric stability under cryogenic temperatures were a concern, further testing was needed.

In the mid 1970's, experience with the first generation cryogenic induction motors revealed some problems [13]. It was identified that the motors were not performing as predicted by the available models for conventional machines. Also, concerns with the dielectric materials stability were confirmed when a number of machines experienced groundwall failures. After extensive testing Nomex paper was found to be the best choice to insulate the iron core from the windings [13]. At the same time turn to turn failures started to happen with these machines in Japan. A significant amount of effort was put forward to study new dielectric materials since the commonly used polyester varnishes at the time, were not able to withstand the transient overvoltages found to be the cause of the failures. Eventually a combination of Polyamide-imide polymers and PET was introduced to insulate the stator conductors with success.

A decade later the US Department of energy funded research to develop a second generation Helium and Hydrogen pump to replace the existing synchronous permanent magnet based machines [16, 17]. Cryogenic induction motors were chosen because of their high reliability and flexibility of operation under a wide range of fluids as well as the resulting thermal management system simplification identified previously. Air-cooled conventional induction motors with a modified copper squirrel cage rotor were tested and implemented at Stanford Linear Accelerator Center operating at 21K (-252.15ºC) for cooling electron beam targets.

Prototype 2.5kW 120000RPM cryogenic induction motor pump was also implemented at Fermi National Laboratory, operating at 5K (-268.15ºC), and used in superconducting magnet cooling system [16]. This new design revealed to be highly reliable, more efficient and simple to both manufacture and perform maintenance. The use of a cryogenic induction motor in cryogenic pumps was, by this point, well established and the next generation magnet cooling systems introduced in Fermi Lab in 1993 were made around this designed [18]. Figure 2.3 shows a cross section view of a centrifugal pump for cooling electron beam targets at Stanford Linear Accelerator Center.

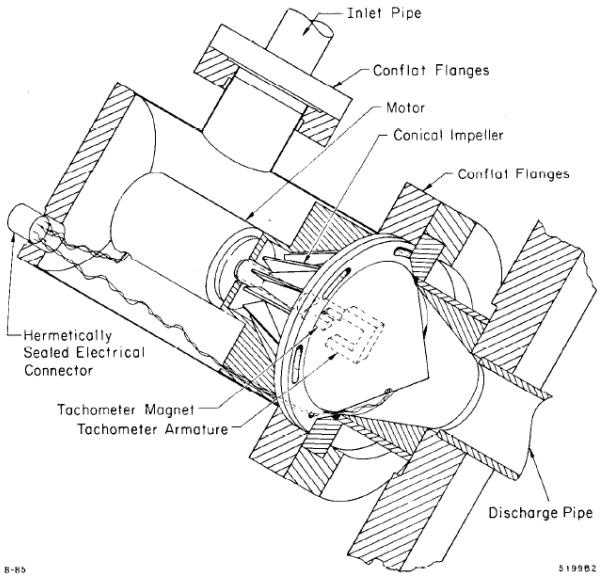

Figure 2.3: Stanford Linear Accelerator Center cryogenic pump assembly [17]

The discovery of high temperature superconductivity (HTS) in 1986 [19] introduced a new application for cryogenic electric machines machines. These superconductors were able to achieve superconductivity at liquid nitrogen temperatures (-196ºC). The combination of HTS stator or rotor coils with cryogenic induction motors was studied extensively, with the possibility of creating a hybrid induction-synchronous motor, where an induction motor with a HTS cage in the rotor could operate either as a traditional induction motor or as a synchronous motor via the Meissner effect [20]. Although tests showed that HTS induction motor is possible and significant performance gains can be made, the hybrid operation revealed to be difficult to achieve [20] and its design inferior to alternative designs using synchronous and reluctance motors [21].

2.2 Recent Developments

Recently research in cryogenic induction motors has been focus in developing models that allow an accurate prediction of electromagnetic phenomena in the cryogenic environment. The Steinmetz steady-state balanced equivalent circuit has been used with good results to predict the overall performance of cryogenic induction motors but it cannot be used in transient analysis and for the prediction

of the distribution of magnetic filed, currents or the effect of rotor motion, essential in the design process. Moreover 3D finite element techniques provide a very detailed and accurate prediction of the electromagnetic phenomena but can be extremely time prohibitive.

In [22] and [23] a time-stepping finite element method for transient analysis in cryogenic induction motors is presented. Here the field model formulation is coupled with the circuit equations that describe winding connections and the magnetic and electrical material temperature dependence to create a more complete model. Also, the rotor motion mechanical equations are coupled to the field and circuit equations via the electromagnetic torque equation. The method presented used a 2D multi-slice formulation with a fixed mesh that is able to accurately compute motor transient results without the time penalty of the classic 3D formulation. The method accuracy was validated using a high-voltage ($U_N = 6.6\mathrm{kV}$) squirrel cage induction motor designed for a LNG pump with $P_N = 785\mathrm{kW}$. The motor no load starting performance was tested at a temperature of 20ºC and -196ºC (using LN_2) and the results of the computation compared with the measured values during the tests. Figures 2.4 and 2.5 show obtained results for current and temperature during no load start.

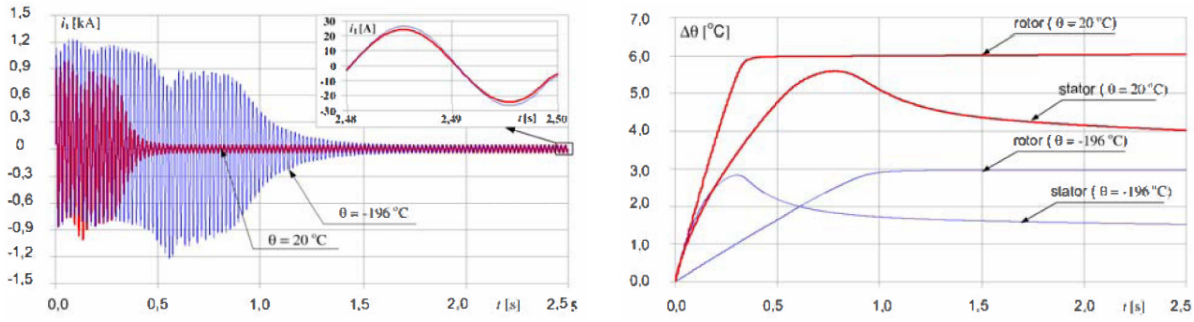

(a)Computed phase current vs. time curves (b)Temperature of stator winding and rotor cage

Figure 2.4: Computed Current and temperature curves [23]

Figure 2.5: Root mean square value of phase currents under no load starting [23]

	Calculations		Measurements	
θ [°C]	20	-196	20	-196
I_1 [A]	17,4	18,6	16,9	18,4

The obtained results showed an error of 3% in the root mean square value of phase currents for 20ºC operation and 1% for -196ºC operation. Furthermore a maximum increase of 5ºC in the stator windings under LNG operation was measured. Despite the good results with significant contribution to motor design its important to point that the accuracy of the method in predicting the behavior and performance of a cryogenic induction motor is still dependent on empirical measurements of the magnetic material $\boldsymbol{B}(\boldsymbol{H})$ curve under cryogenic temperatures. This highlights the need for a pure analytical model capable of computing accurate results based on the magnetic and electrical material properties at ambient

temperature, which have been extensively studied.

In [24] the authors addressed the coupled electromagnetic and thermal analysis of a cryogenic induction motor using a commercially available 2D electromagnetic finite element analysis tool coupled with a 3D lumped parameter thermal network. This approach addresses the problem by emphasizing the computation on the thermal phenomena driving a change in the electromagnetic properties over the contrary, and by not considering windage and friction losses in the computation. Nonetheless, the validation of the model was done using a 15kW induction motor submerged in liquid nitrogen with good results, both electrical and temperature values were computed with an error smaller than 10%. The obtained results are shown in Figure 2.6

	Frequency (Hz)	Voltage (V)	Current (A)	Output Power (kW)
Sim.	90	380	25.8	15.0
Mes.	90	380	30.3	15.0

(a)Rated parameter results

Thermocouple No.	Rated Load Temperature (°C)	
	Mes.	Sim. (Ave.)
#1	-180.9	-185.6
#2	-176.2	-175
#3	-167.5	-175
#4	-160.1	-174
#5	-164.6	-176.9

(b)Temperature results

Figure 2.6: Comparison of obtained results using the method in [24]

In [25] a new method of designing cryogenic induction motors is presented. This new method uses the conventional design method based on the sizing equation D^2L [26] and the finite element formulation shown in[23] to size an ambient temperature version of a motor based on the required design specifications for cryogenic operation. This initial design is then changed based on the assumption that the current density per slot area of the stator and rotor slots is increased by the same rate as the decrease in resistivity of the copper and aluminium conductors. The proposed design algorithm and sizing comparison is shown in figure 2.7 for a 37kW induction motor.

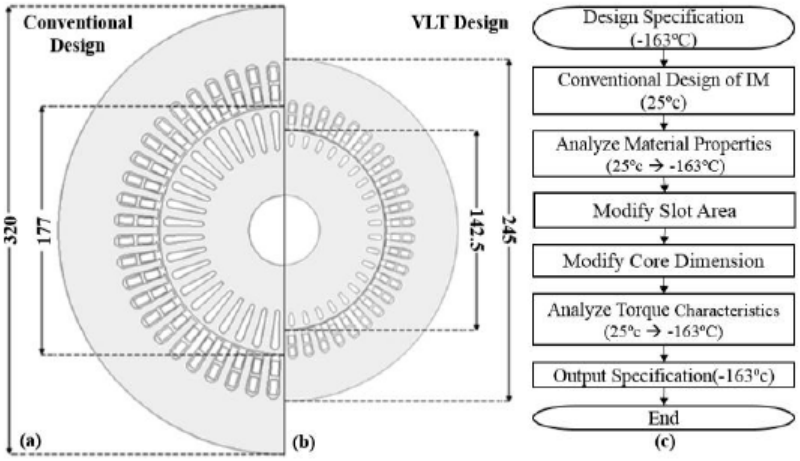

Figure 2.7: Design algorithm and result [25]

The obtained cryogenic design was then built and tested to validate the results. The resultant torque vs speed characteristic and features of merit are shown in figures 2.8 and 2.9.

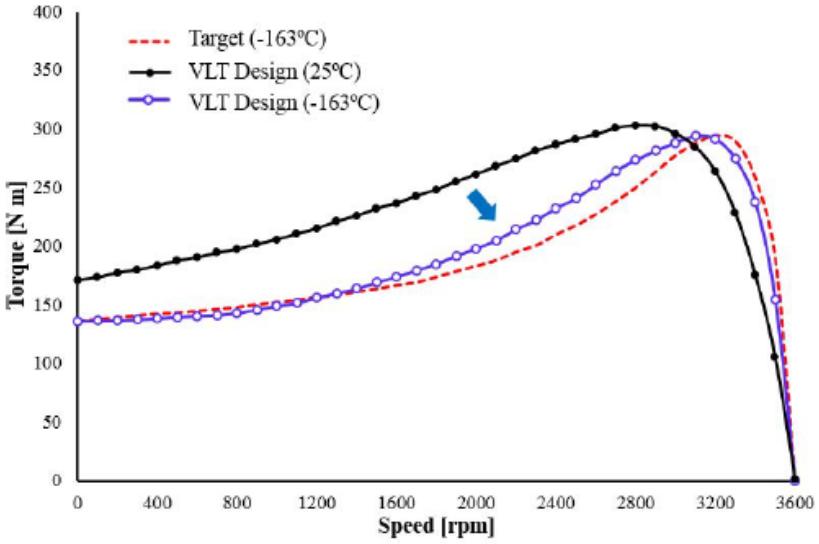

Figure 2.8: Torque vs speed characteristic[25]

Design type	Rated Output	Starting Torque	Efficiency
Target	37kW	137Nm	88 %
Conventional (Simulated)	37kW	81.57Nm	90.23%
VLT (Simulated)	37kW	137.1Nm	91.1 %
VLT (Measured)	37kW	137.5Nm	88.8 %

Figure 2.9: Comparison of motor performance at -163ºC[25]

The method proved to be a significant contribution to the design of cryogenic induction motors, not only were the targets met with great accuracy but also proved that important torque density increases

can be made with cryogenic motors, the final design of this motor was 41% smaller in volume compared with the ambient temperature version with the same ratings.

In addition to the developed of analytical models that try to predict the behavior of an induction motor in the cryogenic environment, recent research as been focused on the determination of iron losses in this environment. The general consensus is that these losses increase in the cryogenic environment but a wide range of increase rates have been proposed, making the estimation of iron losses difficult. In a bid to solve this problem [27] tested eight different silicon steel grades from a range of manufacturers, thicknesses and categories (Oriented grain, Non-oriented grain and amorphous). By fitting the obtained empirical data to the classic loss separation method from [28], it was found that the increase of losses range from 8% to 243%, with an average value of 20%. Also hysteresis losses were found to be relatively constant while eddy current losses increase by the same rate as the conductivity of the silicon steel sheets, in general 20%. The increase of iron losses in cryogenic environment is therefore concluded to be mainly due to the increase of conductivity and as a consequence the eddy current losses [27].

In the last two decades the major players in the aerospace sector, led by NASA have been centering their attention in researching high power density electric motors for propulsion systems [29]. The need to reduce carbon emissions and higher efficiencies has been considered as the driving force behind this research. High speed synchronous and reluctance motors, have been in the forefront of these efforts, either as conventional air cooled machines, cryo cooled or superconducting ones, due to their high torque capability and efficiency [30]. Figure 2.10 shows NASA's Electric Aircraft Testbed project currently in construction.

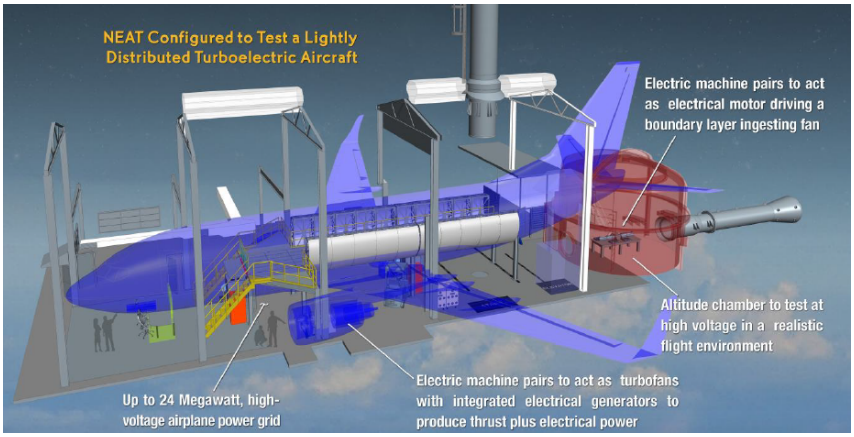

Figure 2.10: NASA Electric Aircraft Testbed (NEAT) project [30]

In the last decade, NASA has shifted research interests from PM synchronous motors to new designs of high power (1MW+ class) induction motors citing safety and robustness concerns of PMSM designs [31]. In 2019 a major breakthrough was made when Ohio State university in partnership with NASA developed a out-runner type air-cooled induction motor with a very high power density outperforming advanced PM synchronous motors. This new motor broke the normalized continuous operation power density record previously held by a Siemens's PM motor using very expensive cobalt based magnetic materials with a continuous operation power density of 2.05 W/kg.rpm. This new induction motor set a

record of 2.6 W/kg.rpm for continuous operation power density and an induction motor power density record of 4.7 kW/kg using of-the-shelf materials. This breakthrough led a team of experts from ARPA, NASA, Boeing, Raytheon,Hyper Tech, Ohio State University and Tennessee Tech University engineers to propose a LNG cryogenically cooled version of this motor as a alternative to the expensive and high risk superconductor machine designs, with the objective of being capable of achieving a power density of over 20kW/kg [11]. This project with a funding of 2.9 million dollars is currently being tested and the results expected in three and a half years.

Following this recent research interests, this thesis dissertation will contribute for a further consolidation of cryogenic induction machines by performing experimental characterization of the performance of cryogenic induction machines and by establishing analytical models to support the experimental findings.

Chapter 3

Electromechanical Performance of Cryogenic Induction Machines

In this chapter the effect of cryogenic conditions on the performance of induction machines will be discussed. The steady-state equivalent circuit model of the induction machine is used to evaluate the effect of the temperature and skin effect, under cryogenic conditions. Lastly, results are obtained based on this model for the torque and efficiency characteristics.

3.1 The Induction Machine in Cryogenic Conditions

Cryogenic temperatures are usually defined as the range of temperatures from -150ºC to -273.15ºC [32]. This range of temperatures is regarded, in science, as one with particular and special properties, and forms a niche, separated, field of study in most, if not all, science disciplines. It is so because these temperatures are significantly lower than those encountered in ordinary physical processes. At these temperatures material properties are changed in ways with very important and interesting consequences, from both the commercial and scientific points of view.

This is also true for induction machines, where the cryogenic conditions have exceptional consequences. In the stator and rotor, conductor resistivity is drastically reduced, which in turn causes a significant reduction in joule losses. Also, this drastic reduction in conductor resistance, coupled with the extreme heat extraction capabilities of cryogenic fluids and systems allow for an increase in motor loading. From this increased motor loading, torque density is also significantly increased, allowing for a reduction in the machines volume when compared with a conventional machine. Nevertheless, there are a few drawbacks worth mentioning. The decrease in material resistivity has the unwanted effect of increasing eddy currents in the iron core of the machine, causing an increase in iron losses, although the increase in iron losses is considerably smaller than the decrease of joule losses. In addition, the presence of a liquid fluid inside the machine causes an increase in windage losses too as well as friction losses in the bearings. The advantages outweigh the disadvantages though and significant efficiency, output power and torque improvements can be made.

3.2 Steady-state electromechanical model

To understand the impact of cryogenic operation in conventional induction motors, the performance of an induction motor is first characterized based on the equivalent electric circuit. These preliminary results intend to show the influence of the parameter's variation with the change of temperature and skin effect. After this analysis, the numerical results will be compared with experimental ones, obtained in section 5. The single phase equivalent circuit parameters determination method was used. This equivalent circuit originally proposed by Steinmetz [33] is the standard in today's electric machine steady-state and balanced analysis since it models the induction machine electrical steady state behavior with enough accuracy, using a lumped parameter model, without an exhausting and complex modeling and computation process. Also, it allows an easy determination of the machine's parameters based on experimental tests. It is obvious that more complex non linear phenomena cannot be modeled this way, granted they still exist, but by considering linear regions of operation these phenomena influence can be minimized and even neglected. In this section, the influence of the temperature and skin effect on the motor's parameters are analysed. For this, the following induction motor equivalent circuit shown in Figure 3.1 is considered.

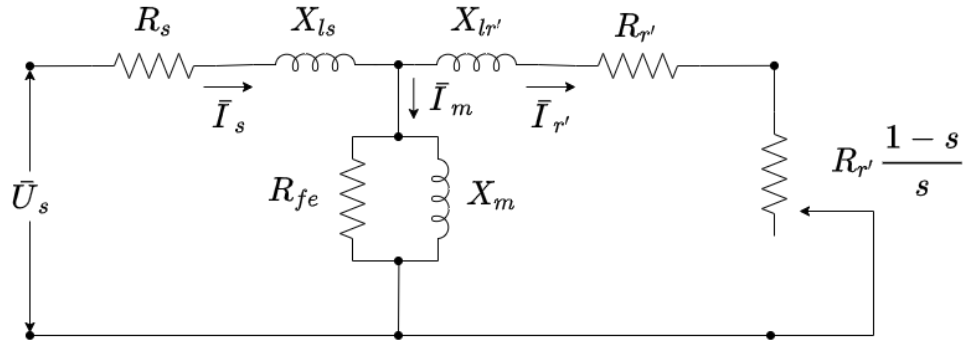

Figure 3.1: Single phase induction motor equivalent circuit

Where:

- $\bar{U}_s$ - Stator voltage
- $\bar{I}_s$ - Stator current
- $\bar{I}'_r$ - Rotor current referred to stator
- $\bar{I}_m$ - Magnetizing current
- R_s - Stator windings resistance
- X_{ls} - Stator leakage reactance
- X'_{lr} - Rotor leakage reactance referred to stator
- R'_r - Rotor resistance referred to stator

- R_{fe} - Equivalent iron losses resistance
- X_m - Magnetization Reactance

3.2.1 Influence of Temperature on the equivalent circuit parameters

In this subsection the influence of temperature in the equivalent circuit parameters is analysed. Starting with the equations for these parameters, this analysis will go through the physical quantities that play a role in this influence and explain to what extent this influence occurs.

Most physical properties of a material or a system are influenced by temperature, from chemical reactions to macro thermodynamic processes. This influence in an electric machine is mainly due to the variation of electrical conductivity of the materials used to build the machine.

Stator resistance R_s

The parameter stator resistance R_s models the physically measurable DC resistance of the stator conductors made out of copper. This resistance is a function of the material resistivity ρ, its length l and A, the cross-sectional area of the conductor and is given by:

$$R = \rho \frac{l}{A} \tag{3.1}$$

While it is true that any of these physical quantities are influenced by temperature to some extent, the influence in the conductor length and cross-sectional area, due to contraction, is very small compared with the influence of temperature in the material resistivity, thus is usually neglected.

The estimation of a material resistivity as a function of temperature is usually done using the well known one term linear equation 3.2.

$$\rho = \rho_0(1 + \alpha(T - T_0)) \tag{3.2}$$

with

$\rho -$ The material's resistivity at a given temperature

$\rho_0 -$ The material's resistivity at the reference temperature

$\alpha -$ The material's temperature coefficient

$T_0 -$ The reference temperature

$T -$ The conductor's temperature of interest

This is done so, because most materials have a linear relationship between resistivity and temperature for a wide range of temperatures. For the case of copper, the cryogenic temperature range where the tests were to be performed, were well within the linear region, according to empirical data [34], and so the relation could be used.

Figure 3.2 shows the resistivity vs temperature curve for copper using data from [34]

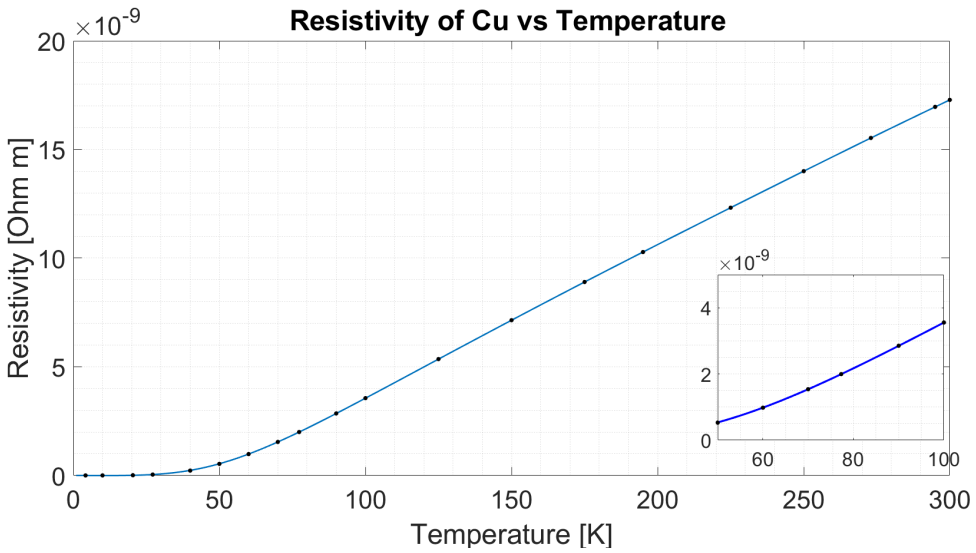

Figure 3.2: Copper resistivity vs temperature

Assuming a copper temperature coefficient $\alpha_{cu} = 0.00386°\mathrm{C}^{-1}$ for the reference temperature of 20ºC (293.15K) and considering that for 20ºC the resistivity of copper is $\rho_0 = 1.68 \times 10^{-8}\ \Omega\mathrm{m}$ [35] it follows that by using equation 3.2 :

$$\rho(T = -196°\mathrm{C}) = 1.68 \times 10^{-8}(1 + 0.00386(-196 - 20)) = 2.7928 \times 10^{-9}\Omega\mathrm{m} \tag{3.3}$$

Meaning that the resistivity of copper ρ_{cu} at 77K is 6.02 times lower than for 293.15K or 20ºC. And since from equation 3.1 it is known that the resistance of the copper conductors is directly proportional to the resistivity of copper, it follows that the DC resistance of the stator copper windings R_s must drop around 6 times when placed in liquid nitrogen.

Rotor resistance R'_r

The parameter R'_r models the resistance of the rotor cage as seen from stator. Since the rotor cage is made out of aluminium, one can say that in a similar manner to the stator resistance R_s, it too is affected by temperature. One may thing that the analysis of the change in resistivity with respect to temperature for the case of aluminium follows the same procedure as done for the stator copper windings, but in fact it does not. This is because, when it comes to aluminium, the relation between resistivity and temperature for temperatures lower than 100K is non linear, meaning that equation 3.2 cannot be used. Nonetheless this analysis is possible by making use of empirical data from [36].

Figure 3.3 shows the aluminium alloy 2024-0, used in this thesis's induction motor, resistivity vs temperature curve

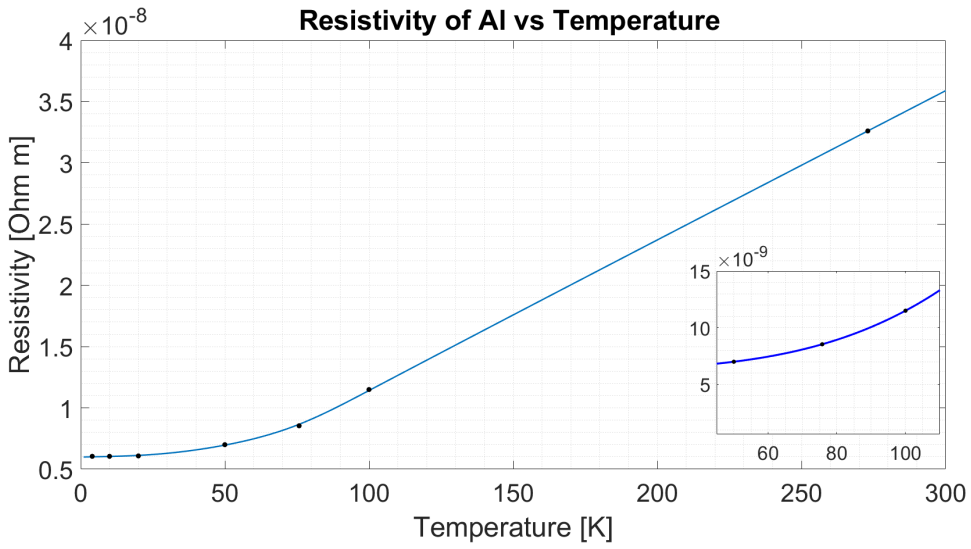

Figure 3.3: Aluminium resistivity vs temperature

From the empirical data it is possible to estimate the aluminium resistivity for the range of temperatures of interest in this thesis, by fitting a third degree polynomial function. The result of this fit is given by 3.4

$$\rho(T) = 7.742 \times 10^{-15} T^3 - 5.025 \times 10^{-13} T^2 + 2.99 \times 10^{-11} T + 5.793 \times 10^{-9} \tag{3.4}$$

$$50\text{K} \leq T \leq 100\text{K}$$

Using equation 3.4 it follows that the resistivity of aluminium for 77K (-196ºC) is

$$\rho(T = 77\text{K}) = 8.6598 \times 10^{-9} \Omega\text{m} \tag{3.5}$$

And since for 20ºC the resistivity of aluminium alloy 2024-0, is [36]

$$\rho(T = 20°\text{C}) = 3.4900 \times 10^{-8} \Omega\text{m} \tag{3.6}$$

One can estimate that the resistivity of aluminium for 77K is 4.03 lower than that for 20ºC, thus the DC resistance of the rotor cage seen from the stator R'_r should also be 4.03 lower when in cryogenic operation.

Equivalent iron losses resistance R_{Fe}

The equivalent iron losses resistance R_{Fe} models the iron core losses in the induction machine. The iron core in these electrical machines can be made out of a wide range of ferromagnetic materials. These different ferromagnetic materials are usually classified by grade, as they differ in many aspects, from impurities content, to grain size and orientation and even by the cutting process used in manufacturing. The use of different types of ferromagnetic materials means that the result of the analysis of the influence of temperature in the iron core greatly varies. Despite this, the average influence across the

most common used grades of ferromagnetic materials is usually considered in the literature when an estimation of the effect is needed [37].

From the literature it is know that the effect of temperature in the iron core is due, for the most part, to the increase of conductivity of the ferromagnetic materials σ and to a smaller extent the magnetic flux density $\boldsymbol{B}$. From Bertotti classical loss separation model [28, 38, 39] its know that the losses in the iron core P_{Fe} can be separated into two distinct groups, the hysteresis losses P_h and eddy current losses P_e, given by equation 3.7

$$P_{Fe} = P_h + P_e \tag{3.7}$$

From previous experiments [37] hysteresis losses P_h are said to be constant with respect to temperature when the iron core is not saturated, this is the case for the machine tested in this thesis.

When it comes to eddy current losses P_e, experimental data shows that these losses are directly proportional to the ferromagnetic material's conductivity, and so an estimation of the impact of temperature in these losses must include an estimation of the increase in magnetic core's conductivity at cryogenic temperatures.

Usually for room temperature operation a linear relation between conductivity and temperature is used to estimate the change in conductivity with respect to temperature, but this relation is not valid in cryogenic temperatures, where non linear effects are present. Therefore empirical data must be used to estimate this effect. According to [37] the increase of conductivity for the most common ferromagnetic materials at 77K compared to ambient temperature of 20ºC (295K) is [10-20%] and as such the equivalent iron losses resistance R_{Fe} should also decrease by [10-20%].

Stator leakage reactance X_{ls}

This parameter models the magnetic energy that does not contribute to the main linked flux between the stator and the rotor. This means that from the total magnetic flux created by the stator coils, some magnetic flux paths close outside the magnetic circuit. These leakage fluxes are mostly due to the geometry of the stator magnetic circuit and the windings connection arrangement. Because of this and as shown experimentally [40] it is usually considered that since the effect of temperature on the machine geometry is negligible (material contraction due to low temperature is negligible, at 77K thermal contraction for aluminium and copper is around 0.4% of its original length at 295K or 20ºC [41]) so is the effect of temperature in the stator leakage reactance X_{ls}, meaning no change in this parameter should be observed.

Rotor leakage reactance, seen from stator $X_{lr'}$

In a similar manner to the case of the stator leakage reactance X_{ls}, this parameter also models a leakage flux component of the total flux produced in the machine, but this time in the rotor magnetic circuit. Furthermore the cause for this leakage fluxes in the rotor is also related to the geometry of the

magnetic circuit of the rotor and thus, no influence of temperature is considered in this parameter as well.

Magnetizing reactance X_m

Magnetizing reactance X_m models the magnetic energy present in the airgap of the induction machine which is the result of the linked magnetic flux between the stator and rotor. From the previous leakage reactances temperature influence analysis it was shown that magnetic properties of the machine's materials are not influenced by temperature, this is also true for this parameter which is therefore assumed constant.

3.2.2 Influence of the Skin effect on the equivalent circuit parameters

The skin effect is a electrodynamic phenomena where the distribution of current in a conductor cross section is non uniform. When a direct current flows in a conductor it is distributed uniformly throughout the conductor cross-section. On the other hand, a time varying current flowing through a conductor creates a non uniform current distribution, with most current flowing in the peripheral area of the conductor, hence the name "skin effect". This non uniform distribution of current, reduces the cross sectional, current carrying, area within the conductor, effectively reducing the conductor's cross sectional area and hence increasing its resistance. Furthermore the decrease of the effective conductor cross-sectional area also acts to decrease the conductor's inductance.

This section concerns the analysis of the skin effect on the equivalent circuit parameters. Here it is going to be shown that the skin effect can have a significant impact on some parts of the machine and negligible on others, both negative and positive, which alters the performance of the machine and thus its equivalent circuit parameters. Furthermore its not possible to characterize the influence of the skin effect without including the effect that temperature has on conductivity, for which the skin effect is strongly dependent.

To aid in the analysis of the skin effect influence, one should start by introducing the concept of skin depth δ. The skin depth δ is defined as the depth below the conductor surface at which the current density falls to $\frac{1}{e}$ of the surface current density, and is given by equation 3.8, in the quasi-static regime ($\epsilon\omega << \frac{1}{\rho}$)

$$\delta = \sqrt{\frac{2\rho}{\omega\mu}} \tag{3.8}$$

with

$\rho -$ The material's resistivity at a given temperature

$\omega -$ The angular frequency of current

$\mu -$ The magnetic permeability of the conductors

Furthermore by comparing the skin depth value with the conductor size one can infer to what extent does the skin effect act in the flow of current.

Stator resistance R_s and stator leakage reactance X_{ls}

To analyse the influence of the skin effect in the stator resistance R_s and the stator leakage reactance X_{ls}, one should start by computing the skin depth δ for a copper conductor in the ambient and cryogenic temperature conditions.

First considering a temperature of 20ºC, it is known that the resistivity of copper is $\rho_{Cu}(20°\mathrm{C}) = 1.68\times 10^{-8}\ \Omega\mathrm{m}$ [35]. Also considering the relative magnetic permeability of copper $\mu_{rCu} = 0.999994 (\mu_{Cu} = 1.256629 \times 10^{-6}\mathrm{H/m})$ and the grid frequency of $f = 50\mathrm{Hz}$.

$$\delta = 0.0092\mathrm{m} = 9.2\mathrm{mm} \tag{3.9}$$

For the case of cryogenic temperature operation, as seen in the previous section the conductivity of copper should increase 6 times. This increase in conductivity causes a decrease in the skin depth, increasing the influence of the skin effect on the conductors. As computed in equation 3.3 the copper's resistivity at 77K is $\rho_{Cu}(77K) = 2.7928 \times 10^{-9}\Omega\mathrm{m}$. Furthermore magnetic permeability μ is considered to be constant, with respect to temperature, and as such the relative magnetic permeability is equal to $\mu_{rCu} = 0.999994 (\mu_{Cu} = 1.256629 \times 10^{-6}\mathrm{H/m})$. Computing the skin depth δ for this temperature, we get the following result in equation 3.10

$$\delta = 0.0038\mathrm{m} = 3.8\mathrm{mm} \tag{3.10}$$

Since the stator conductors diameter is typically lower than 1mm and the skin depth (field penetration distance) is more than 3 times larger, for the worst case scenario, meaning cryogenic temperatures, one can consider that the skin effect has no influence both on the stator resistance R_s and also on the stator leakage reactance X_{ls}.

Equivalent iron losses resistance R_{Fe} and magnetizing reactance X_m

The analysis of the influence of skin effect in the equivalent iron losses resistance R_{Fe} and the magnetizing reactance X_m follows a similar process as the one for R_s and X_{ls}. This is because just like in the stator slots conductors, the iron core of the machine is also made out of dozens of conductors isolated from each other, in the form of silicon-iron (for this case) lamination's with a thickness of up to 1.5mm (usually less than 1mm). Despite this fact, the electric and magnetic properties of the core silicon-iron alloy are very different from those of copper, mainly the magnetic permeability that is, at 20ºC, $\mu_{Cu} = 1.256629 \times 10^{-6}\mathrm{H/m}$ for copper and $\mu_{FeSi} = 5 \times 10^{-3}\mathrm{H/m}$ for FeSi, meaning almost 4000 times larger for the case of FeSi.

As a first approach in this influence analysis, the computation of the skin depth for silicon-iron under an ambient temperature of 20ºC and a cryogenic temperature of 77K is presented in equations 3.11 and 3.12. For 20ºC a resistivity value of $\rho_{FeSi} = 4.72 \times 10^{-7}\Omega\mathrm{m}$ [42] is used and a relative magnetic permeability value of $\mu_{rFeSi} = 3979\ (\mu_{FeSi} = 5 \times 10^{-3}\mathrm{H/m})$.

$$\delta = 7.7522 \times 10^{-4}\mathrm{m} = 0.7752\mathrm{mm} \tag{3.11}$$

For the case of cryogenic temperature, at 77K, the ratio between the resistivity of the FeSi and pure iron Fe at 20ºC is used to estimate the resistivity of the FeSi core at 77K, meaning that this ratio is assumed to be constant and independent of temperature. Using the previous assumption, we get a resistivity ratio $\frac{\rho_{FeSi}}{\rho_{Fe}} = 4.9116$, and since the resistivity of pure iron, at 77K, is $\rho_{Fe} = 0.6 \times 10^{-8}\Omega\mathrm{m}$ [43] it follows that the resistivity of FeSi is $\rho_{FeSi} = 2.9470 \times 10^{-8}\Omega\mathrm{m}$. Equation 3.12 shows the computed skin depth value for the iron core lamination's in cryogenic temperature.

$$\delta = 1.9371 \times 10^{-4}\mathrm{m} = 0.19371\mathrm{mm} \tag{3.12}$$

Since the iron core lamination's thickness is around 0.5mm it is expected that under ambient temperature operation the skin effect influence is small, but can be significant for machines with a lamination thickness of around 1mm. For the cryogenic case, this influence is expected to be important and cannot be neglected. This influence is going to be explored and validated trough experimental tests as this effect is usually neglected and an analytical model is not available.

Rotor resistance R'_r and rotor leakage reactance X'_{lr}

In squirrel cage induction motors the rotor circuit is rather different from the stator one, the main difference being that contrary to the stator slots, rotor slots are fully filled by a solid conductors called the rotor bars. Since in the stator case the skin effect is negligible, due to the fact that the stator slots are filled with small diameter conductors isolated from each other (with a fill factor of around 40%) it is predictable that in the rotor side the skin effect is very important and cannot be neglected. Another major difference in this particular machine is that the rotor bars are made out of aluminium which has a higher resistivity than copper, as seen in section 3.2.1.

As a first estimation of the influence of the skin effect in the rotor bars one should compute the skin depth. From equation 3.6 the aluminium resistivity for 20ºC is $\rho_{Al} = 3.49 \times 10^{-8}\Omega\mathrm{m}$. Furthermore relative magnetic permeability of aluminium is $\mu_{rAl} = 1 (\mu_{Al} = 1.256665 \times 10^{-6}\mathrm{H/m})$. Equation 3.13 shows the result of the skin depth computation for aluminium at 20ºC

$$\delta = 0.0133\mathrm{m} = 13.3\mathrm{mm} \tag{3.13}$$

For cryogenic temperature (77K), and using the resistivity value for aluminium from equation 3.6, the following skin depth value is obtained

$$\delta = 0.0066\mathrm{m} = 6.6\mathrm{mm} \tag{3.14}$$

From equations 3.13 and 3.14, and since the height of the conductor is in the order of 1cm for this particular machine, it is apparent that the skin effect influence is important, especially in the cryogenic regime of operation.

The quantification of the skin effect influence in the equivalent circuit parameters is done by computing two coefficients, the resistance correction coefficient K_R, defined as the ratio between the the AC and DC resistance of a conductor and the inductance correction coefficient K_L, defined as the ratio between the AC and DC inductance of a conductor.

The computation of these two correction coefficients is not straightforward though, a simple close solution is possible for rectangular or trapezoidal slots common in high power machines, but a general solution involves a more complex iterative method. The method used in this thesis is know as the multilayer approach method, and was introduced in [44–46]. The multilayer approach method consists of dividing the rotor bar into n layers with height $h_p = \frac{h_t}{n}$, width b_p and length l_{stack} as shown in figure 3.4.

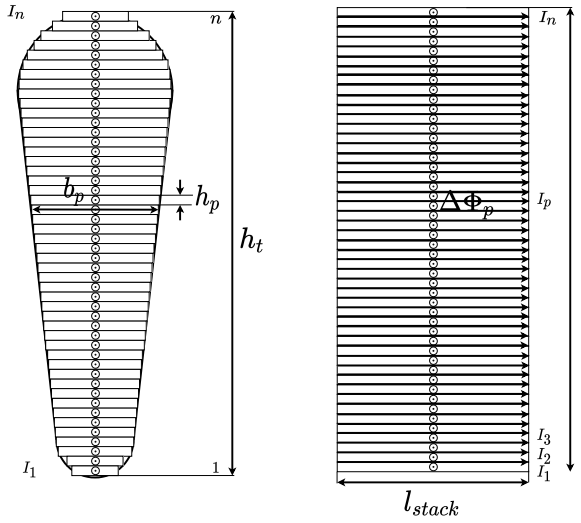

Figure 3.4: Division of solid conductors into layers

Applying Faraday's law to the p^{th} layer, results in equation 3.15

$$R_p\bar{I}_p - R_{p+1}\bar{I}_{p+1} = -js\omega\Delta\bar{\phi}_p \tag{3.15}$$

where s is the slip and R_p represents the resistance of the p^{th} layer and is given by equation 3.16

$$R_p = \frac{l_{stack}}{\sigma_{Al} b_p h_t} \tag{3.16}$$

With R_{p+1} the resistance of the $(p+1)^{th}$ layer and $\Delta\bar{\phi}_p$ the leakage flux flowing between the p^{th} and $(p+1)^{th}$ layers.

This leakage flux $\Delta\bar{\phi}_p$ is dependent on the flux density $\boldsymbol{B}_p$ in layer p, which in turn depends on the magnetomotive force (current linkage) computed from the bottom of the slot up to layer p.

The flux density $\boldsymbol{B}_p$ is therefore given by equation 3.17

$$\boldsymbol{B}_p = \mu_0 \frac{MMF}{b_p} = \mu_0 \frac{1}{b_p} \sum_{k=1}^{p} \bar{I}_k \tag{3.17}$$

And the leakage flux $\Delta\bar{\phi}_p$ given by equation 3.18

$$\Delta\bar{\phi}_p = \boldsymbol{B}_p l_{stack} h_p = \mu_0 \frac{l_{stack} h_p}{b_p} \sum_{k=1}^{p} \bar{I}_k \tag{3.18}$$

From equation 3.18 its possible to define the p^{th} layer's inductance L_p as

$$L_p = \mu_0 \frac{l_{stack} h_p}{b_p} \tag{3.19}$$

Substituting equation 3.18 and 3.19 into equation 3.15, and solving for the $p+1$ current $\bar{I}_{p+1}$ yields

$$\bar{I}_{p+1} = \frac{R_p}{R_{p+1}} \bar{I}_p + j \frac{s\omega L_p}{R_{p+1}} \sum_{k=1}^{p} \bar{I}_k \tag{3.20}$$

Now, since the total current in the slot I_b is know, a priori, one can define the estimation of the initial current $\bar{I}_1$ at the bottom layer as

$$|\bar{I}_1| = \frac{I_b}{n} \tag{3.21}$$

One can, now, use equation 3.15 to compute the current in all the layers n

$$I'_b = |\sum_{p=1}^{n} \bar{I}_p| \tag{3.22}$$

Once the layer currents $\bar{I}_1$,..,$\bar{I}_n$ are know, it follows that the total AC losses in the rotor bar is given by equation 3.23

$$P_{ac} = \sum_{p=1}^{n} |\bar{I}_p|^2 R_p \tag{3.23}$$

Additionally, by defining the uniformly distributed DC current I_{pDC} in layer p as

$$I_{pDC} = \frac{I'_b}{A_{bar}} h_t b_p \tag{3.24}$$

it follows that the DC power loss P_{DC} in the slot is given by equation 3.25

$$P_{DC} = \sum_{p=1}^{n} I_{pDC}^2 R_p \tag{3.25}$$

Therefore, the skin effect resistance correction coefficient K_R, can be computed using equation 3.26

$$K_R = \frac{P_{ac}}{P_{DC}} = \frac{\sum_{p=1}^{n} |\bar{I}_p|^2 R_p}{\sum_{p=1}^{n} I_{pDC}^2 R_p} \tag{3.26}$$

Concerning the skin effect inductance correction coefficient K_L, its computation is done by computing the magnetic energy in the slot.

The AC magnetic energy in the slot W_{mAC} is given by equation 3.27

$$W_{mAC} = \frac{1}{2}\sum_{p=1}^{n} L_p |\sum_{k=1}^{p} \bar{I}_k|^2 \tag{3.27}$$

Furthermore, the DC magnetic energy in the slot W_{mDC} is

$$W_{mDC} = \frac{1}{2}\sum_{p=1}^{n} L_p |\sum_{k=1}^{p} I_{kDC}|^2 \tag{3.28}$$

Finally it follows that the skin effect inductance correction coefficient K_L is given by equation 3.29

$$K_L = \frac{W_{mAC}}{W_{mDC}} = \frac{\sum_{p=1}^{n} L_p |\sum_{k=1}^{p} \bar{I}_k|^2}{\sum_{p=1}^{n} L_p |\sum_{k=1}^{p} I_{kDC}|^2} \tag{3.29}$$

With the skin effect correction coefficients computed, the AC resistance and inductance is given by

$$R_{AC} = K_R R_{DC} \tag{3.30}$$

and

$$L_{AC} = K_L L_{DC} \tag{3.31}$$

Note : As this method approximates the slot shape using an arbitrary number of layers n, the summation result I_b' in equation 3.22 is most likely different from the total current in the slot I_b. In this case the value of the obtained layer current should be multiplied by $\frac{I_b}{I_b'}$ to get their real values.

Applying the multilayer approach method to the rotor slots gives the following results.

For ambient temperature operation, with a temperature of 20ºC, the skin effect correction coefficients K_R and K_L values are

$$K_R = 1.0058 \tag{3.32}$$

and

$$K_L = 0.9986 \tag{3.33}$$

For a temperature of 77K(-196ºC) yields

$$K_R = 1.0545 \tag{3.34}$$

and

$$K_L = 0.9867 \tag{3.35}$$

From these results its expected that the influence of skin effect under ambient temperature should be small, increasing the resistance by 0.58% and decreasing the inductance by 0.14%. When it comes to cryogenic operation (-196ºC) this influence is significant, with the resistance increasing by 5.45% and the inductance decreasing by 1.33%

3.3 Numerical Results

In this section numerical results are to be presented for ambient temperature and cryogenic conditions. Torque and efficiency curves are to be simulated using the experimentally obtained equivalent circuit parameters analysed later in chapter 5. These numerical results are intended to give an estimation of the influence that both temperature and skin effect have in the performance of the machine as a whole.

3.3.1 Temperature influence

Figure 3.5 shows, in black, the torque vs speed characteristic of the induction machine under ambient temperature operation. In red, the torque vs speed characteristic for the induction machine under cryogenic temperature, here it is assumed that the whole machine is at the same temperature of 77K. And, in blue, the torque vs speed characteristic in cryogenic temperature but this time assuming that the rotor temperature is at 97K, 20K higher than the stator. This later assumption is a common one in motor performance analysis for machines under ambient temperature operation. This does not imply that in cryogenic operation the rotor is also 20K above the stator, indeed it is not as discussed, later, in chapter 5. Nonetheless it is used here to give an idea of the influence of temperature in the machine's performance.

From figure 3.5 and looking at the black and red curves it is apparent that temperature has a very significant impact in the torque production throughout the whole range of slip. First, the most obvious difference is the maximum torque. For ambient temperature peak torque is around 1.72Nm, at a rotor speed of 585RPM while in cryogenic temperature (whole machine at 77K) peak torque is around 3.56Nm at a rotor speed of 1191RPM. Meaning that peak torque is 2.0698 times bigger in the cryogenic regime than in ambient temperature (relative difference of 106.98%). Furthermore peak torque speed is increased 2.036 times (relative difference of 103.59%) in the cryogenic regime compared to ambient temperature.

This behavior is expected, as peak torque production is regulated by the ability to convert magnetic energy into mechanical work. Under ambient temperature, and since the induction machine studied here has a very low nominal power, joule losses dominate. This means that by simply cooling the stator and rotor, one can drastically reduce joule losses hence increasing power output. Its important to note that while in ambient temperature the machine is thermally unstable when the load demand is higher than the nominal point of operation, its expected that, in cryogenic operation, this does not happen, as liquid nitrogen is able to maintain a stable temperature even at loads close to peak torque.

Another clear difference between the black and red curves is the starting torque. As observed in the simulations the starting torque of the machine in 77K is lower than the one in ambient temperature operation, with an expected starting torque of 1.59Nm for ambient operation and 1.52Nm for cryogenic operation, meaning a decrease of 4.403% in the starting torque.

The reason for this lower starting torque is twofold. First, the resistance reduction due to temperature, both in stator and rotor circuits means that the impedance seen from the stator is significantly lower in

cryogenic operation. This lower impedance seen from the stator will cause a large starting current to flow, around 20A in cryogenic operation and just shy of 10A in ambient temperature. This larger starting current will cause a significant voltage drop in the stator windings which reduces magnetizing voltage and thus the magnetic flux produced by the stator. Added to this effect is the fact that a lower rotor resistance R'_r implies that the effect of the rotor leakage reactance X'_{lr} is larger and so the induced currents in the rotor will have a significant phase shift relative to the induced emf in the rotor, i.e the rotor power factor is low, causing a decrease in the linked flux between stator and rotor (relative to ambient temperature where the rotor resistance value is closer to the rotor leakage reactance). The resultant flux in the airgap, as the result of the interaction between stator and rotor magnetic flux is therefore lower and so is the starting torque.

Looking at the blue curve in figure 3.5, the rotor resistance influence is apparent. Since the rotor is in this case at 97K, 20K higher than the stator, its expected that the starting torque is higher than that of the red curve, where the entire machine was considered to be at 77K, and indeed it is, the starting torque in this case is 1.74Nm, 14.4737% higher. Furthermore it is also higher than in ambient temperature operation (an increase of 9.4340%), meaning that while there isn't a significant difference in stator losses relative to the red curve case, and despite the expected higher losses in the rotor due to the higher resistance, the resultant linked flux between the rotor and stator must be greater and the improved rotor power factor dominant in the start up operation.

Another difference between the the red and blue curves is the slip at which peak torque is produced. From the analysis of the single phase steady state equivalent circuit its expected that peak torque is independent of the rotor resistance R'_r and the simulations show that it is, no difference in peak torque is seen in the simulation data. However, and as clear in the simulation result, the increase in the rotor resistance acts to increase the peak torque slip, or analogously, a decrease in the peak torque rotor speed N_r, the blue torque characteristic is therefore a parallel shifted version of the red curve, meaning the machine's electrical constant is increased.

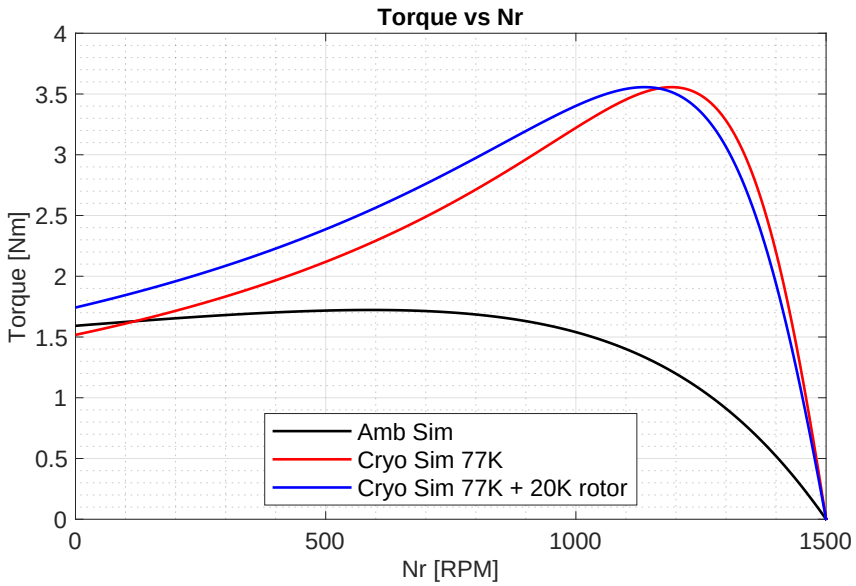

Figure 3.5: Torque temperature influence

Regarding efficiency, from figure 3.6 it's expected that the maximum, for ambient temperature operation, is $\eta = 64.15\%$ at a rotor speed of $N_r = 1358\text{RPM}$ while for cryogenic operation $\eta = 85.9\%$ is expected, at a rotor speed of $N_r = 1443\text{RPM}$. An absolute increase of 21.75% is ,therefore, expected. This significant increase is mainly due to the decrease in the stator losses, which dominate the losses in these very low power induction machines. This lower stator losses means that more electric power is converted into mechanical work which is clear in figure 3.7

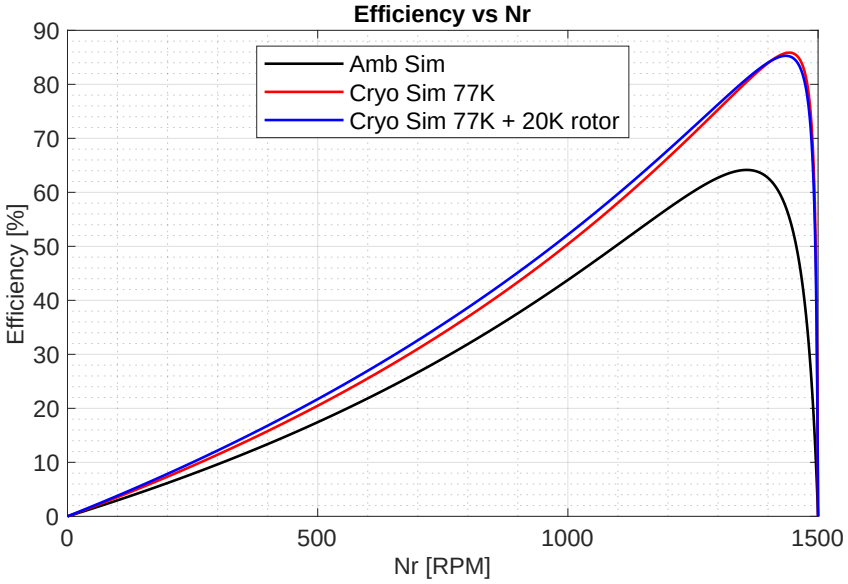

Figure 3.6: Efficiency temperature influence

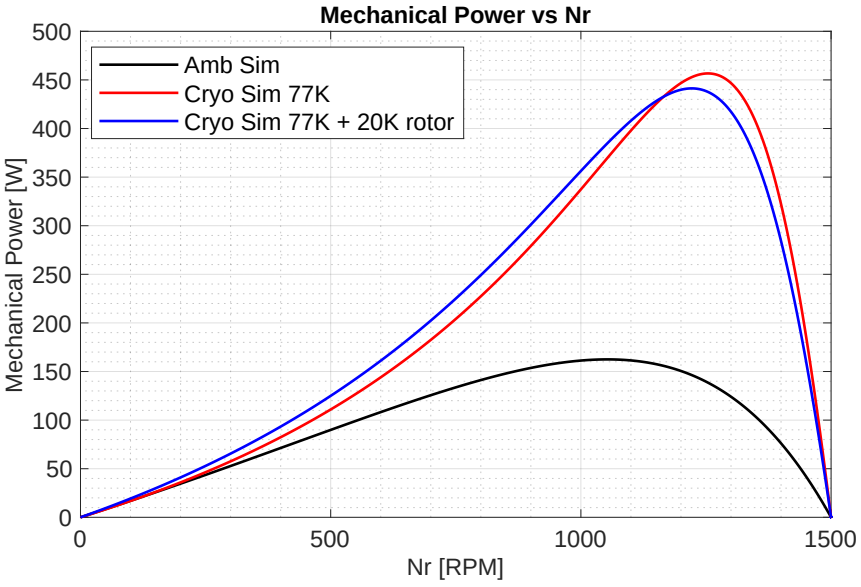

Figure 3.7: Mechanical power temperature influence

3.3.2 Skin Effect influence

In figure 3.8 four curves are presented, in black the baseline torque vs speed characteristic for the induction motor at 77K with no skin effect considered, in red is added the skin effect influence to the black curve. The blue curve represents the torque characteristic assuming that the rotor is at 97K and no skin effect is present and finally the green curve is the same situation as the blue curve, but this time with skin effect included.

It is clear from figure 3.8 that the skin effect influence is significant when slip is close to 1 and negligible when slip is close to 0. This is expected since the frequency of rotor currents is a function of slip and is given by equation 3.36

$$f_r = sf_s \tag{3.36}$$

the maximum frequency of rotor current is therefore when $s = 1$, which means that the penetration depth δ is, at this point, at its minimum value. This minimum value of δ is lower than the rotor slot high, the skin effect is present and so the rotor AC resistance R'_r increases, this effect is clearly observed in figure 3.9

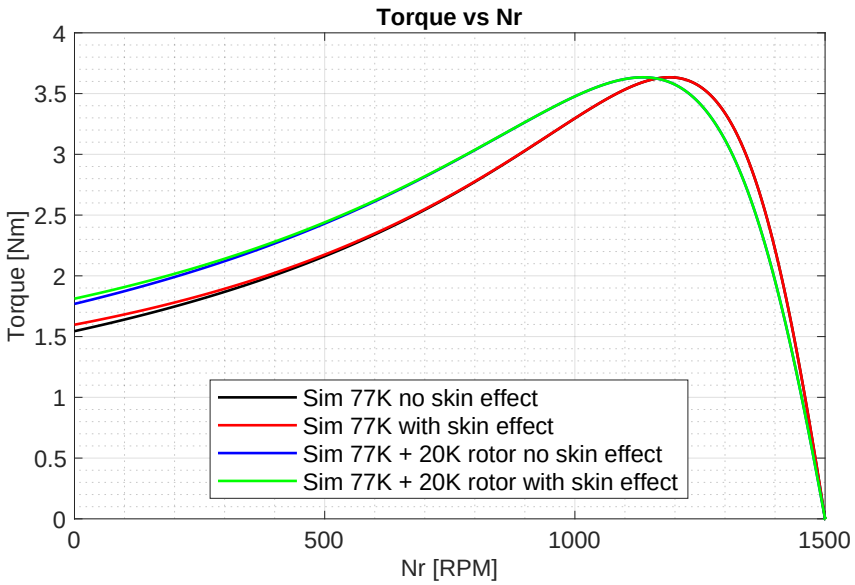

Figure 3.8: Torque skin effect influence

This increase of the rotor resistance R'_r causes an increase of start up torque as previously explained. Taking a look at the start up torque of the black curve compared to the red one, there is an increase of 3.49 % in the start up torque due to do skin effect (1.55Nm to 1.6Nm). This increase is 2.25% when the rotor is at 97K, a smaller increase compared to the case where the whole machine is at 77K due to the increased resistivity of aluminium.

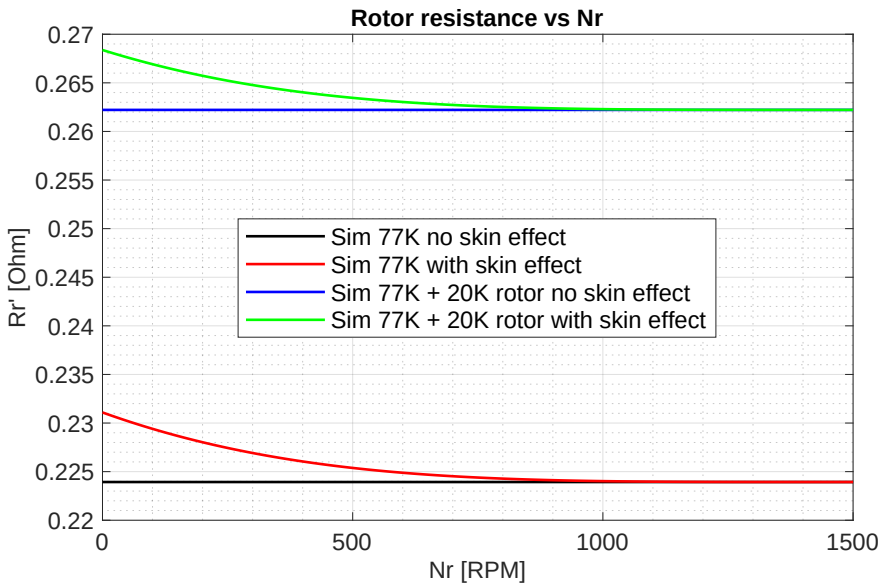

Figure 3.9: Rotor resistance skin effect influence

Figures 3.10 and 3.11 show that the influence of the skin effect on the efficiency and mechanical power is negligible, in fact the maximum increase of efficiency due to skin effect is around 0.8%, again for slip close to 1.

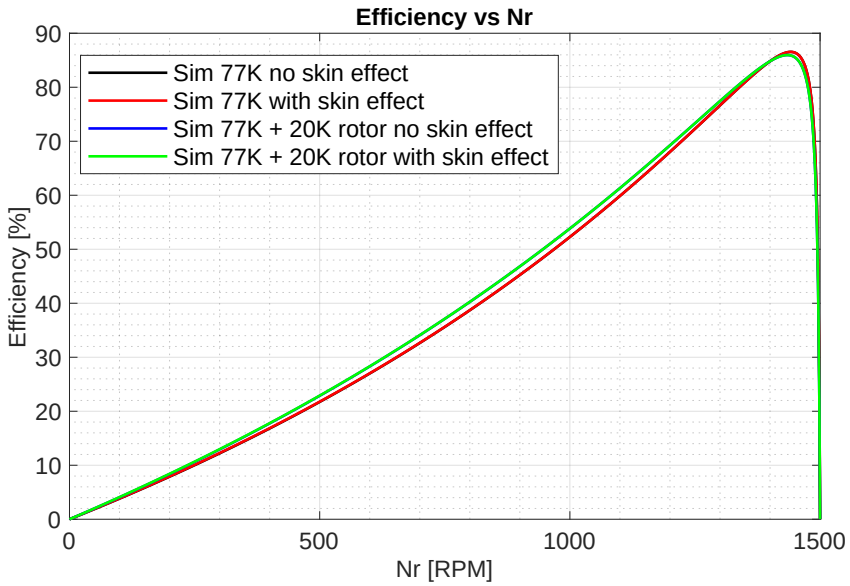

Figure 3.10: Efficiency skin effect influence

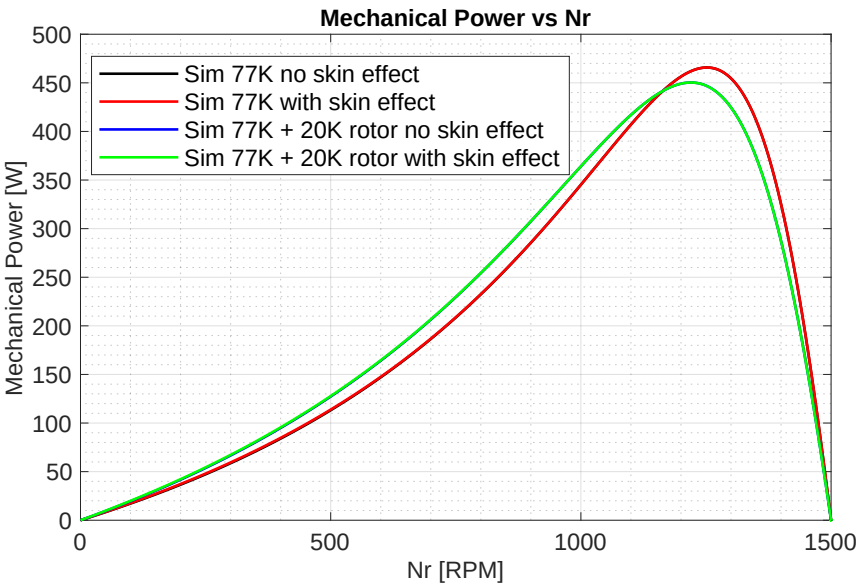

Figure 3.11: Mechanical power skin effect influence

Chapter 4

Experimental Setups and Methodology

There are two main set up typologies that one may use, when doing load tests and both no load and blocked rotor test, a vertical set up and a horizontal one. In conventional machine operation, where the machine is tested and operated in ambient temperatures, the choice of the set up type is straightforward and a horizontal set up is most likely the choice, given its simplicity and the lack of need for a more complex structure needed for a vertical setup. In cryogenic conditions there is an added element that must be taken into careful consideration, the presence of liquid nitrogen. While a horizontal set up with a LN_2 container is definitely possible to build, it would mean using expensive solutions to guarantee that liquid nitrogen spills and losses be minimized, like cryogenic seals. With this in mind, it was decided to follow a vertical solution, where the induction machine is immersed in liquid nitrogen.

With this decision taken into consideration, there are a few points to consider:

- Nitrogen container is to be manually filled, meaning, there is no active circulating system for cooling the machine
- Nitrogen inlet must be thermally isolated from the rest of the setup, mainly from the metal structure components
- Nitrogen vapor needs to be vented out of the LN_2 container to avoid pressure build up
- LN_2 container axle opening must ensure minimum nitrogen loss
- Structure components must be thermally isolated from the LN_2 container and machine to avoid influence of the temperature in the DC Generator, acting as a load
- LN_2 container volume must be minimized to minimize nitrogen usage
- Machine height must be adjustable

Considering the last points, two experimental setups were built, one with a 240W DC machine acting as a load, Figure 4.1 (b), and other with a 1000W DC machine, Figure 4.1(c). The second set-up was

developed, as an improved test bench, to achieve higher torque values from the induction machine. A description of the overall setup-structure is shown in Figure 4.1(a), where the main equipment are the liquid nitrogen vessel, the induction motor and a DC machine acting as a load.

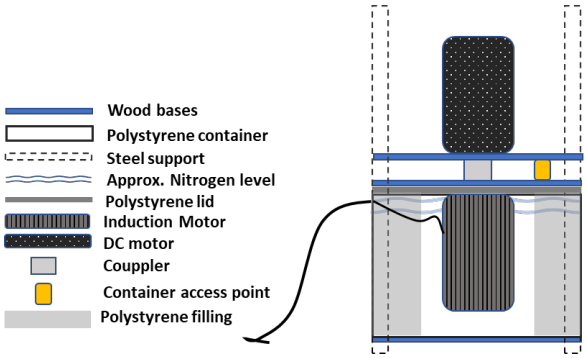

(a) Setup diagram

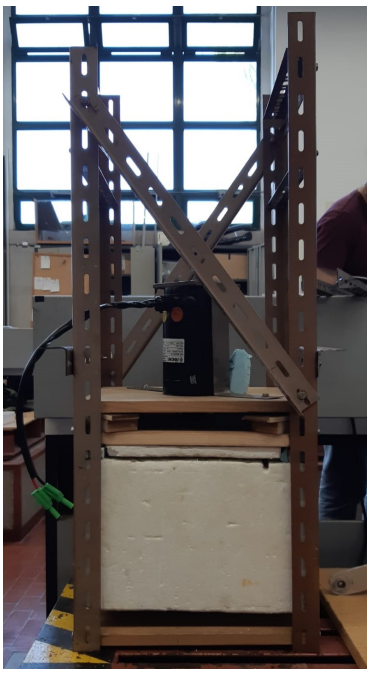

(b) Setup structure 1

(c) Setup structure 2

Figure 4.1: Experimental setup

4.1 Experimental Setup

4.1.1 Experimental set up 1

As can be seen from Figure 4.1(b), the structure is based on a truss, made of steel, wood and polystyrene materials, which are of easy access and low costs. To test the induction machine under different loads, a DC machine is used. In this set-up a 240W 24V DC machine was used, with the characteristics listed in Table 4.1.

Table 4.1: Rated values for DC generator 1

	DC Generator 1 Nameplate
	Armature Circuit
Voltage	24 V
Current	10 A
Power	240 W
Speed	2000 RPM
Torque	1.15 Nm

Please note that, at first glance, from the electrical point of view, the structure seems to have no influence whatsoever. However, being a coupled electrical and mechanical system, there will always be some influence, and for the experiments in this thesis, that influence comes mainly from mechanical vibrations. This is not a problem when using specialized and heavy setups but, for this case, the structure rigidity is important. This is because vibrations can cause misalignment in the rotor shafts coupling, which not only cause losses in the mechanical power transfer between the IM and load but also excess force being applied to the machines bearings, possibly causing catastrophic failure of the bearings or most likely the appearance of a ”stray” load in the experimental results, lowering efficiency.

It is therefore important to test the structure to see if there are excess vibrations. With vibrations taken care of the next step and one of the most important is the sealing of the LN_2 container. As it was decided to build the LN_2 container using purely a polystyrene box (for the sake of speed and cost) it is difficult to seal it properly. It is important to note that in reality, a completely sealed LN_2 container of this kind is extremely dangerous, since as heat is transferred from the machine to liquid hydrogen, it causes nitrogen to change phase, going from liquid to gas, which obviously expands and increases the pressure inside the vessel, which can be a hazard. It is therefore of the most importance that the LN_2 container building assures that a controlled leak is maintained throughout the experiment, and leakage losses be minimized.

As the first tests showed, this sealing process is rather difficult. The difficulty comes from the fact that the usual sealing silicon, tapes, epoxies, etc don’t work in these extreme temperatures, so a solution had to be found.

After experimenting, the best way to seal the LN_2 container was using thin strips of polystyrene, edged between the LN_2 container’s body and the lid, as well as using a thick double sided tape for a

better seal, while maintaining some leakage to avoid increase of pressure.

4.1.2 Experimental set up 2

This second experimental setup is introduced by the need to test the induction motor with higher loads. In fact, the 240W DC machine power cap was quickly reached, soon after increasing the current beyond nominal value at ambient temperature. By increasing the stator current to 6 A(60% above nominal current at ambient temperature), the output power at the DC generator was already 240W, limiting the tests.

With this in mind it was clear that, a higher power for the generator acting as a load was required. The 1kW 1500 RPM DC machine presented in Figure 4.2 was used, with the characteristics listed in Table 4.2.

Figure 4.2: 1kW separate excitation DC machine

Table 4.2: Rated values for DC Generator 2

	DC Generator Nameplate	
	Armature Circuit	**Field Circuit**
Voltage	230 V	220 V
Current	4.4 A	0.55 A
Power	1000 W	
Speed	1500 RPM	
Torque	6.37 Nm	

This new generator allowed to test the induction machine up to 1000W loads, five times bigger than the previous DC generator. As this machine is much heavier than the previous one, building a new

structure that would couple to setup 1 and allow the machine to be in the vertical position was needed. The new machine weighs about 30kg, this fact turned out to make the structure building process quite difficult. The difficult part was not building a strong enough steel structure, materials and tools to do it were available, but rather install the new machine into this, also new, structure. Regarding the choice of structure design to build, the choice was the half bridge type structure presented in Figure 4.3.

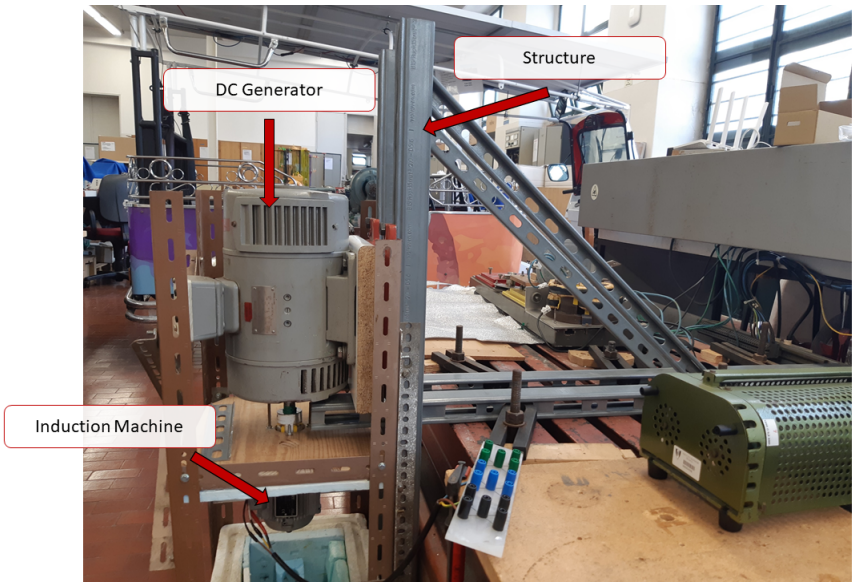

Figure 4.3: Experimental set up 2 structure

This structure was optimized to make use of the laboratory working benches, as it can be seen in figure 4.3. The structure is anchored in the elevated base using heavy steel clamps that were tightened using screws. This provided a very good anchor point but one still had to prevent the structure from rotating. For this purpose two steel supports were screwed to form a triangle, as seen in the picture. These supports allowed to control the angle of the main beams where the DC machine was to be mounted, this fine tuning was needed to ensure that both machines were coupled as straight as possible. With a straight and solid structure the mounting of the machine base (in red) was straightforward. Figure 4.4 shows a detailed diagram of the structure and its components.

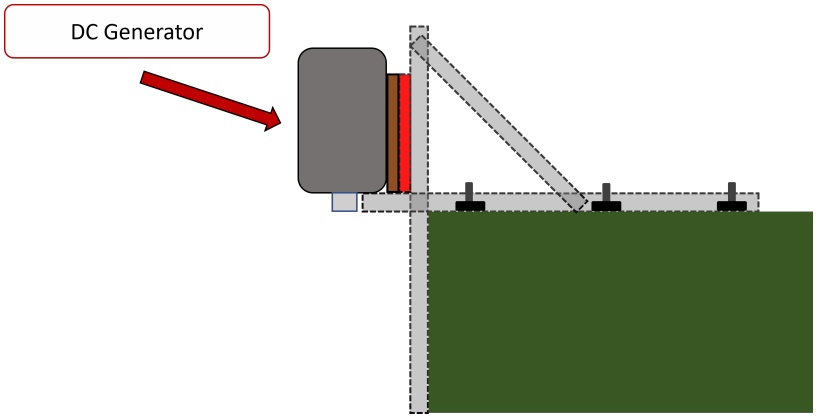

Figure 4.4: Experimental set up 2 structure diagram

4.1.3 Measuring Set Up 1 and Setup 2

As described before a powerflow analysis was needed to fully describe the workings of the problem in question. There are both AC and DC signals in this set up, AC in the motor side and DC in the load side. The following paragraph describes the flow of power through the set up.

The induction motor is fed by the grid through an auto-transformer to control the stator voltage. Since the axle (rotor) of the IM is mechanically coupled to the DC generator's axle (armature), mechanical power is transferred from the IM to the DC generator. To control the load of the induction motor, the DC generator is connected to a variable resistive load. Also as the second DC generator is of the separately excited type, a DC power source is needed to generate the excitation field.

The diagram in figure 4.5 describes the general connections and set-up.

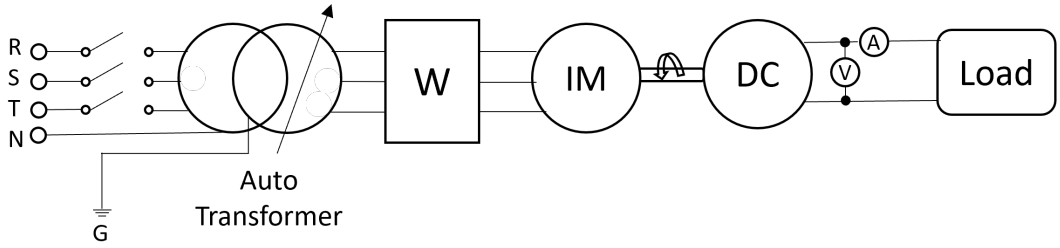

Figure 4.5: Experimental setup Connection diagram

In this set-up the following quantities were recorded:

DC Generator:

- U_a - DC generator's armature voltage
- I_a - DC generator's armature current
- I_f - DC generator's field current current

Load:

- U_{load} - Voltage at the load terminals
- I_{load} - Load current

Induction Machine:

- U_s - Phase voltages(Phase 1,2 and 3)
- I_s - Phase currents(Phase 1,2 and 3)
- P_{active} - Active power in each phase
- N_r - Rotor angular velocity

This measurement was difficult for the smaller 240W DC generator setup in cryogenic temperatures but rather simple in ambient temperatures. For the second setup it was simple in both conditions.

The difficulty in the first case stems from the fact that the smaller machine was asymmetrical when it comes to the axle, meaning that the machine's axle was only accessible through one side of the machine, while the other side was completely blocked off. This means that the only way to measure angular velocity was to use the accessible axle, where the coupler was. This was fairly easy in ambient temperatures, with the aid of reflective tape, but impossible in cryogenic temperature as, in this later case, the area around the coupler was full of ice crystals and water vapor which scattered the light impulse from the tachometer. Figure 4.6, where the top wood base (DC generator base) is removed, shows this effect clearly.

Figure 4.6: Ice build up in the coupler surroundings

In the case of the second experimental setup, the DC generator has an accessible axle from both sides of the machine, this allowed measuring the angular rotor velocity far from the cold side of the machine, and therefore away of the cold vapor and ice deposits. Therefore by using the reflective and black tapes in the accessible axle end, the rotor angular velocity could be measured without any problem.

Furthermore, since the wattimeters used in the first setup had a maximum current rating of 10A, a new wattimeter was made using current and voltage transducers and a DAQ system. An image of the final wattimeter circuit is shown in figure 4.7.

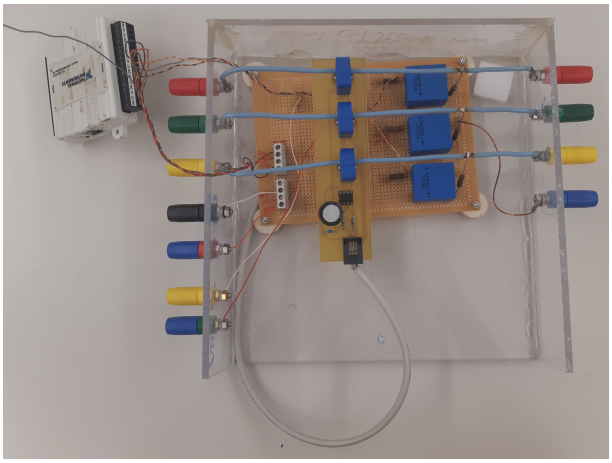

Figure 4.7: Wattimeter circuit

4.2 Bearings Preparation

Bearings performance is many times overlooked when analyzing these types of motors in ambient temperature. As a fundamentally mechanical structure, an electrical engineer will often times, see it as a structural component of an electric motor, just like the stator casing. In reality, bearings are an influential part of the electric motor performance as they are a significant part of mechanical losses, and thus efficiency gains can be made just by choosing a more suitable bearing for the specific application where the motor is to be working on. Also the bearing's lubricant (grease) is also very important, as there is a plethora of different types, natural or synthetic, for low temperatures or high temperatures, different types of loads etc. For this study, the choice of the type of bearings and grease are not only important but also crucial. This is, as expected, due to the very low temperatures that the machine is to be tested under.

Most lubricants used today can handle a very wide spectrum of temperatures, usually from -50ºC up to 200ºC [47] or even higher temperatures. The same can be said for the types of materials and geometries of the bearings themselves. Since this motor is to be run at around -196ºC (77K), this choice must be carefully made, and have in consideration, the cost, availability, thermal amplitude sensitivity, no load and load friction coefficients.

The Induction motor studied in this thesis is a custom motor from Lafert, with standard bearings of the deep groove ball bearing type, made by SKF and built from stainless steel, with model number 6201-2Z [48], Figure 4.8 shows a close up image of the bearings used. The exact composition of the bearing's

Figure 4.8: IM's bearing SKF 6201-2Z

grease was not known, SKF recommends a mineral oil type grease named LGHP 2 for this type of motor under ambient temperatures, which have a temperature of operation between -40ºC to 150ºC [49].

4.2.1 Testing the bearings

From SKF information, the lubricant used in these types of bearings was not compatible with temperatures below -40ºC. Nonetheless testing the performance of the bearings in liquid nitrogen is essential to identify and solve any unexpected behavior and possible problems that might occur under such extreme temperatures, for this the following tests were performed:

- Liquid nitrogen bath until completely cooled
- Bearing rotation test

This test is rather simple, a small polystyrene container was filled with liquid nitrogen. Next the bearing is submerged into the liquid nitrogen, and after 4 minutes the system is at thermal equilibrium. Figure 4.9 shows an image of the liquid nitrogen bath with a bearing.

Figure 4.9: Bearing cryogenic test

After thermal equilibrium the bearing is removed from the polystyrene container and smooth rotation of the bearing is checked. This rotation is checked by clamping the outer surface of the bearing using a plastic clamp, rendering it unmovable and using an appropriate glove to manually rotate the inner surface, as shown in figure 4.10

Figure 4.10: Bearing rotation test

This can be done using a small motor also, but a manual process was chosen because, it is simple to do, its much easier to listen as well as feel ice crystals cracking this way (in reality, this is where most

of the information from this test comes from, the cracking of the ice crystals is very easy to ear and feel) and its generally faster.

With no modifications whatsoever to the bearing, it quickly freezes in the liquid nitrogen bath. This cannot be visually seen while the bearing is still inside the liquid nitrogen but by removing it and checking rotation, there is no movement from the bearing at all. Furthermore, by forcing the bearing to rotate, a lot of cracking is heard. This cracking indicated that there were solid crystal inside the bearing.

4.2.2 Cleaning the bearings

After the first experiments it was clear that the bearing's grease was freezing, thus blocking any rotational movement of the bearing, the bearings needed to be cleaned.

Cleaning the bearings turned out to be a long task, because the bearings were sealed and could not be opened, making the removal of the grease very difficult.

Due to the sealing, the only option was to slowly clean the grease in an Acetone/Diluent bath. The acetone slowly propagates into the bearing and removes the grease. To accelerate this process, the bearing is rotated when fully submerged, by rotating it, the grease sips out of the bearing via the centrifuge effect, also using a syringe to force acetone into the bearing works well combined with the bearing rotation. Rotation of the bearing is done for about 30 min, and by hand. This works very well as a first step towards a clean bearing as it takes most of the grease out but it is not enough. The problem is that even a seemingly residual content of grease can get the bearing stuck and lead to a lot of mechanical losses. Figures 4.11 a) and b) show this process in action.

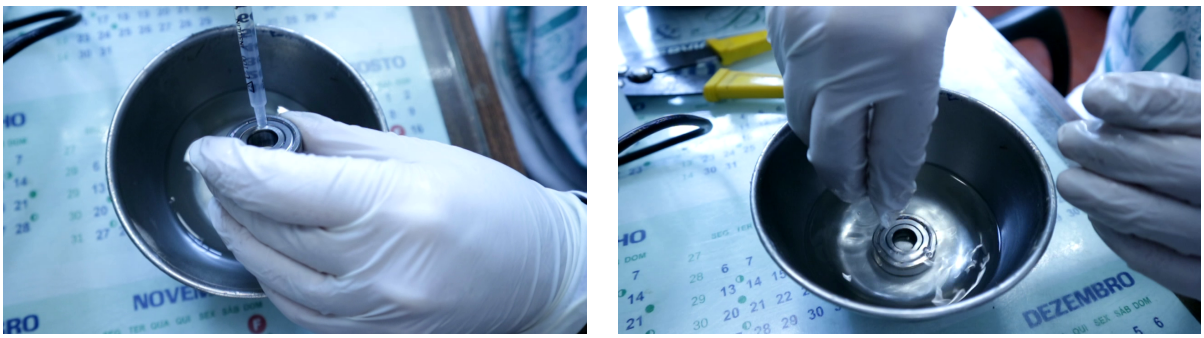

(a)Injecting acetone (b) Acetone bath

Figure 4.11: Bearings cleaning process

The solution is to let the bearing inside the acetone bath for about 5 days to a week, this was the time it required to completely clean out every residue of grease. It is important to add that every day the acetone should be changed, and that throughout these 5 to 7 days the bearing was tested many times, as previously explained, until it was possible to rotate it freely with no apparent formation of ice crystals. An important note to add is that while the bearing performs very well when submerged, after just 5 seconds of exposure to the atmosphere, water vapor in the air starts to freeze and a lot of ice crystals are formed, inside the bearing itself, rendering the rotation movement very difficult or even impossible.

In addition it is important to stress that for a reliable operation of the bearings throughout the lifetime of the machine, specifically designed cryogenic bearings should be used. Despite a few attempts at contacting cryogenic bearings manufactures, it was impossible to order some samples in time and so for the purposes of this thesis degreasing the bearings was the only possible solution.

4.3 Motor parameters experimental determination

To experimentally characterize the induction machine operating in cryogenic condition different experimental tests will be conducted, according to IEC 60034-2-1 standard: No-load, Blocked Rotor Tests and Load tests. The No-load tests allows the determination of the magnetizing branch parameters of the equivalent circuit, as well as the rotational losses, and the Blocked-Rotor Tests allows the computation of the stator and rotor impedances. From these, the influence of the temperature and the skin effect on the induction machine can be validated. In addition, load tests are also carried to analyze the improve of performance of the machine when operated in cryogenic conditions.

4.3.1 No-Load Test

The No-Load Test consists of testing the motor in a no load condition, meaning that the load is removed from the setup and the rotor is to spin freely. Under this condition the rotor current is small, but not zero, this is due to the small torque the motor needs to overcome friction losses and spin freely. This means that the input stator current is therefore mainly the excitation current needed to create the rotating magnetic field. In fact, it is generally considered that the rotor current is zero and that the excitation current amplitude is equal to the stator current, the steady-state balanced equivalent circuit therefore simplifies to the circuit in 4.12.

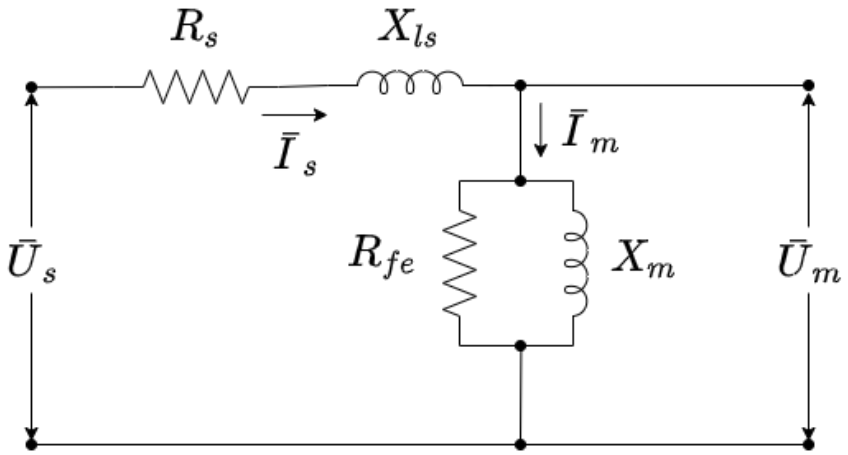

Figure 4.12: No-Load equivalent circuit

At no-load, the active power P_{noload} consumed by the machine is given by 4.1, where P_{cu}, P_{Fe} and P_{mec} are the stator copper losses, iron core losses and the mechanical rotational losses, respectively.

$$P_{noload} = P_{cu} + P_{Fe} + P_{mec} \tag{4.1}$$

Considering the equivalent circuit, it can be translated by

$$P_{noload} = 3R_s I_{sRMS}^2 + \frac{3U_{mRMS}^2}{R_{Fe}} + P_{mec} \tag{4.2}$$

Which means that, knowing the stator and mechanical losses, it is possible to compute the equivalent iron losses resistance

$$P_{noload} - 3R_1 I_{sRMS}^2 - P_{mec} = \frac{3U_{mRMS}^2}{R_{Fe}} \tag{4.3}$$

Since the stator winding DC resistance can be measured using a multimeter or by indirect computation through the $R = \frac{V}{I}$ relationship it follows that the equivalent iron losses resistance is then

$$R_{Fe} = \frac{U_{mRMS}^2}{(P_{noload} - R_s I_{sRMS}^2 - P_{mec})} = \frac{3U_{mRMS}^2}{P_{Fe}} \tag{4.4}$$

The same procedure can be applied when finding the magnetizing reactance X_m, now with the reactive power

$$X_m = \frac{3U_{mRMS}^2}{(Q_{noload} - 3X_{ls} I_{sRMS}^2)} \tag{4.5}$$

Since measuring the coils inductance is not straight forward and since the leakage reactance is typically very small compared with the magnetizing impedance, one can neglect it, and so

$$X_m = \frac{3U_{mRMS}^2}{Q_{noload}} \tag{4.6}$$

As stated previously, the No-Load test also allows one to determine mechanical losses, which are needed to compute R_{Fe} and the IM efficiency.

To compute P_{mec} one has to understand the relationship between the No-Load input power consumed by the machine P_{noload} and the applied magnetization voltage voltage U_m.

As described by equation 4.3 the no load power P_{noload} is proportional to the square of the stator current I_s and the square of magnetizing voltage U_m. This means that for small values of I_s and U_m, close to 0, the copper and core losses are negligible, and in fact the power consumed by the machine in this range of operating values is not zero, or close to it, this non zero DC offset of the Power vs Voltage curve, shown in figure 4.13, is, effectively, only due to mechanical losses. This allows the computation of the maximum mechanical losses value, which is computed for the maximum no load rotor speed of 1495RPM, close to the synchronous speed of 1500RPM.

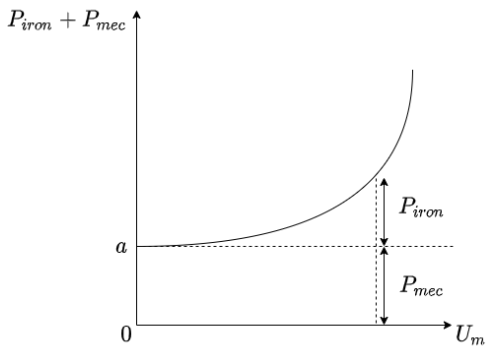

Figure 4.13: No-Load Theoretical P vs V curve

Therefore, using the experimental results, one can do a quadratic fitting with a constant offset, and separate the iron core from the mechanical losses.

$$P_{noload} - P_{Cu} = P_{mec} + P_{Fe} = A + BU_m^2 \tag{4.7}$$

from this, A gives the mechanical losses and B the iron core losses resistance $B = \frac{3}{R_{Fe}}$.

The computation of the magnetizing reactance X_m follows a similar procedure, but now using the reactive power

$$Q_{noload} = \frac{3U_{mRMS}^2}{X_m} = CU_{mRMS}^2 \tag{4.8}$$

Where the magnetizing reactance is determined from parameter $C = \frac{3}{Xm}$.

Test Procedure - No-Load Ambient Temperature

In this section the No-Load test procedure is described. First the load is decoupled from the machine, meaning the load acting DC generator is physically removed from the setup, this is to guarantee that the measured values of power consumed by the machine don't include the DC generator's mechanical losses and residual stray losses, since in this test the objective is to characterize the induction machine itself.

The IM is moved to the top of the structure, removing it from the polystyrene LN_2 container, this step is important because despite not having a coupled load, there are still joule losses heating up the machine. The LN_2 container is a quasi-closed system, there isn't a sufficient airflow inside it to cool down the machine, turning the inside of the LN_2 container into a rather hot environment. A diagram for the No-load test setup modification is shown in figure 4.14.

Electrical connections are made as explained in the experimental setup section. After this, and before starting the test, the stator voltage is slowly increased up to its nominal value using the autotransformer as the objective was to perform the test from nominal voltage down to 0V. This step is crucial to the experiment in order to guarantee consistent and coherent results because as the copper windings temperature increases, so does the windings resistance, and as such one needs to make sure that when

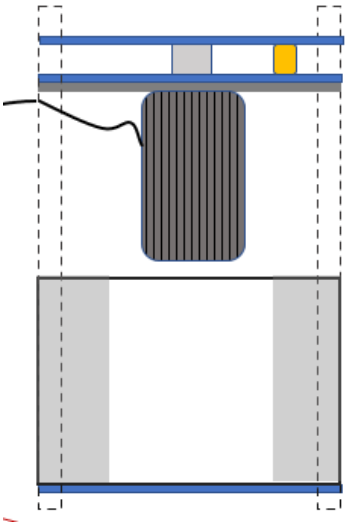

Figure 4.14: No-Load Ambient Operation set up diagram

the test starts, the IM is at its steady state temperature, which implies the copper resistance is also at its steady state value. Otherwise, if the test started from minimum voltage up to its nominal value, resistance would also increase and the results would turn out incoherent.

Steady state temperature is checked using the copper winding's resistance, for this, the machine's power is turn off and the stator winding's resistance measurement is taken using a multimeter, when this value stabilizes steady state temperature is reached and this resistance value measured is taken as the test initial winding resistance, it allows one to indirectly compute the machine temperature, important for the analysis of the results.

After this later step the test can start, during it, the phase currents, phase voltages, active power measurements are taken using the wattimeters. Besides these measurements, rotor speed measurements are also taken at each step, using an optical tachometer and reflective tape in the rotor shaft.

4.3.2 Blocked Rotor Test

The Blocked Rotor Test consists of testing the motor under rated current with its rotor mechanically blocked, to guarantee that the rotor is stationary. This test, analogous to a transformer short circuit test, gives information about stator and rotor leakage reactances and resistances. Under this conditions, as the rotor is blocked, the slip is equal to one, the equivalent mechanical power impedance $R'_r \frac{1-s}{s}$ is therefore zero and so the magnetizing impedance is much larger than the "short circuit" path. This results in the assumption that magnetizing current is negligible and the IM equivalent circuit simplifies to the circuit shown in figure 4.15

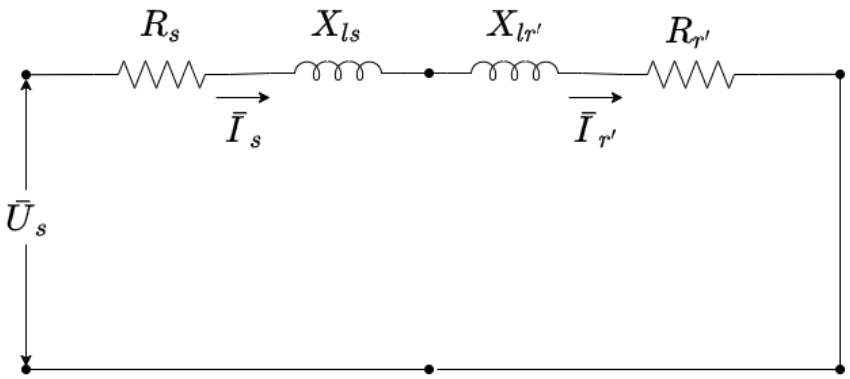

Figure 4.15: Blocked Rotor equivalent circuit

With the assumption previously described, it follows that the magnitude of active power consumed by the machine under the blocked rotor test is given by

$$P_{blockedrotor} = 3(R_s + R'_r)I^2_{sRMS} \tag{4.9}$$

and for the magnitude of reactive power consumed we have

$$Q_{blockedrotor} = 3(X_{ls} + X'_{lr})I^2_{sRMS} \tag{4.10}$$

Both reactive and active power magnitudes are proportional to the square of the stator current. Taken this into account, the power vs current curve can be modelled by quadratic functions and trough the fitting of the experimental results, the rotor and stator parameters can be estimated.

Test Procedure - Blocked Rotor Ambient Temperature

In this section the Blocked Rotor test procedure is described. In this test the load doesn't necessarily need to be decoupled since with the rotor locked in place there is no mechanical power transfer and thus the DC generator doesn't influence the results. Despite this, the DC generator was decoupled, this facilitates moving the IM to its upper position in the structure, just like in the no load test as well as the mechanical locking of the rotor, which is done using a steel rod jammed into the coupler as seen in figure 4.16.

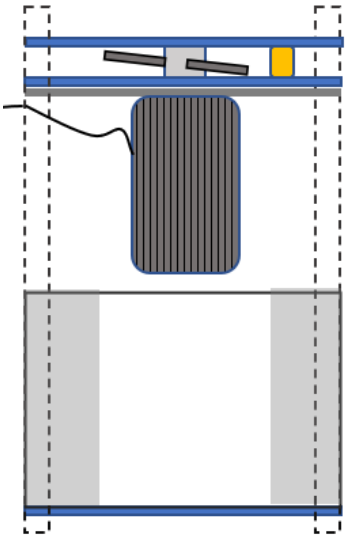

(a) Setup diagram

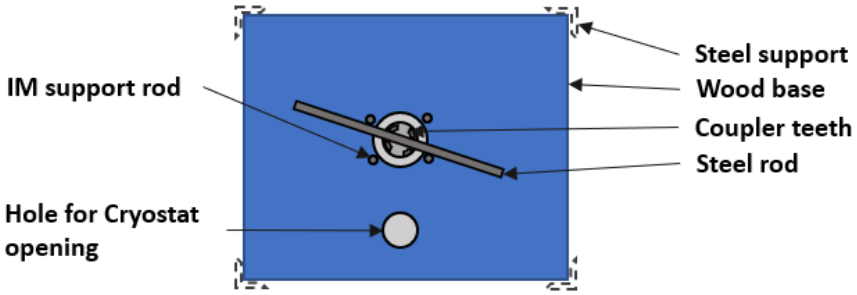

(b) Setup top view

Figure 4.16: Blocked Rotor Ambient Operation set up diagram

Here though, sufficient airflow around the machines outer shell is imperative. Since in this case a very low impedance current path is tested, even a small voltage value at the stator can create very large currents which quickly heat the machine and can cause dielectric thermal failure. This effect is aided by the fact that the autotransformer's voltage control knob, doesn't allow for a smooth commutation of the internal taps controlling voltage values, this can cause one to make more force than needed and end up increasing the voltage too much causing a current spike, special care must be taken.

With all the connections made as showed before, a similar process as in the No-Load is necessary. While in the No-Load case nominal voltage is imposed, in blocked rotor its the nominal current that is imposed, this means that stator voltage is relatively small. By imposing the nominal current one makes sure that motor parameters under nominal load are analysed, not only that, bigger currents can, as explained in the previous paragraph, lead to thermal failure or even saturation of the iron core, influencing the results.

With the nominal current imposed, it is important, once again, that a stable temperature is reached, by doing this and by progressively lowering the current, one makes sure that resistance values do not change throughout the test and results are coherent.

4.3.3 Load Test

The load test consists of testing the motor under rated voltage and frequency, with a mechanical load coupled to the motor shaft. This test is performed to obtain the load performance characteristics of the motor. Here, the motor is tested under a wide range of loads, from the startup to no load conditions. From this test torque, efficiency, power, slip and power factor characteristics are obtained and the machine as a whole is analysed. The following paragraphs describe the procedure used in this test.

Load Test Procedure - Ambient Temperature

Using an autotransformer to step down from three phase grid voltage of 400V (phase to phase) to 40V the nominal phase to phase voltage of the induction machine, the breaker is turned on and the circuit is energized. The machine's temperature is key here, as the conductive parts of the machine heat due to joule losses, resistance increases, as previously noted

The idea is to start the test with the maximum load points and decrease the load slowly, always guaranteeing that steady state operation is reached before measurements are taken. This way, one can guarantee that the measurements taken are done so for constant conductor DC resistance values, this is imperative to maintain coherence throughout the test results.

This fact, and considering that the machine in question is only cooled by a small fan coupled to the rotor shaft, limits the maximum load point of the test, which was chosen to be around the nominal point. Maximum phase current was therefore limited to 3.8A, around 4% over the nominal current, and after reaching steady state operation, rheostat resistance is increased slowly, lowering the load demand, until the machine reached the synchronous speed of 1500RPM. Throughout the test phase voltages, phase currents, active power and rotor speed is measured.

Chapter 5

Results

In this section, the experimental results obtained in both ambient temperature and cryogenic conditions are detailed. From the experimental results, the methodology presented in the modelling chapter is validated. First, the ambient temperature tests are performed to obtain the equivalent circuit parameters at normal conditions, and then, the cryogenic tests are performed to validate the change of these parameters with the cryogenic temperature.

5.1 Problem Description

For a full analysis of the machine performance it is necessary to characterize two distinct environment conditions of operation, they are

- Ambient temperature operation
- Cryogenic temperature operation

Ambient temperature operation is the normal operating condition for any machine, whether it is electrical, mechanical, acoustic, etc. This implies that the machine operates at environment temperature, being cooled only by the forced air flow through the motor fins, as it was designed for.

Cryogenic temperature operation implies running the machine under very low temperatures, which in this case the working temperature is around 77K (-196 ºC). In this work the 77K temperature is set by using liquid nitrogen contained in a semi-sealed vessel.

5.2 Ambient Temperature Test Results

In this section Ambient temperature tests results are analysed. Here Load tests are compared with the simulated torque and efficiency curves, obtained from the parameters extracted using the No-load and Blocked Rotor tests. The results obtained in these tests will act as the baseline case, from which the later experimental results are to be compared. Figure 5.1 shows an image of the IM in ambient temperature conditions.

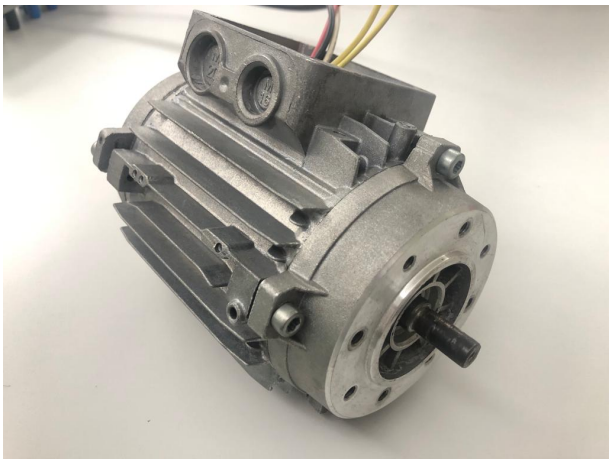

Figure 5.1: IM in Ambient temperature

5.2.1 No-Load Test

Following the test procedure previously detailed, the first ambient temperature tests were performed. In figure 5.2 are shown, in dots, the experimental points obtained for the iron and mechanical losses and the reactive power, as a function of the machine magnetizing voltage, and in a continuous line the interpolation. In figure 5.3 is shown the segregation of losses, where the iron and mechanical losses are computed from the induction machine input active power and removing the stator copper losses.

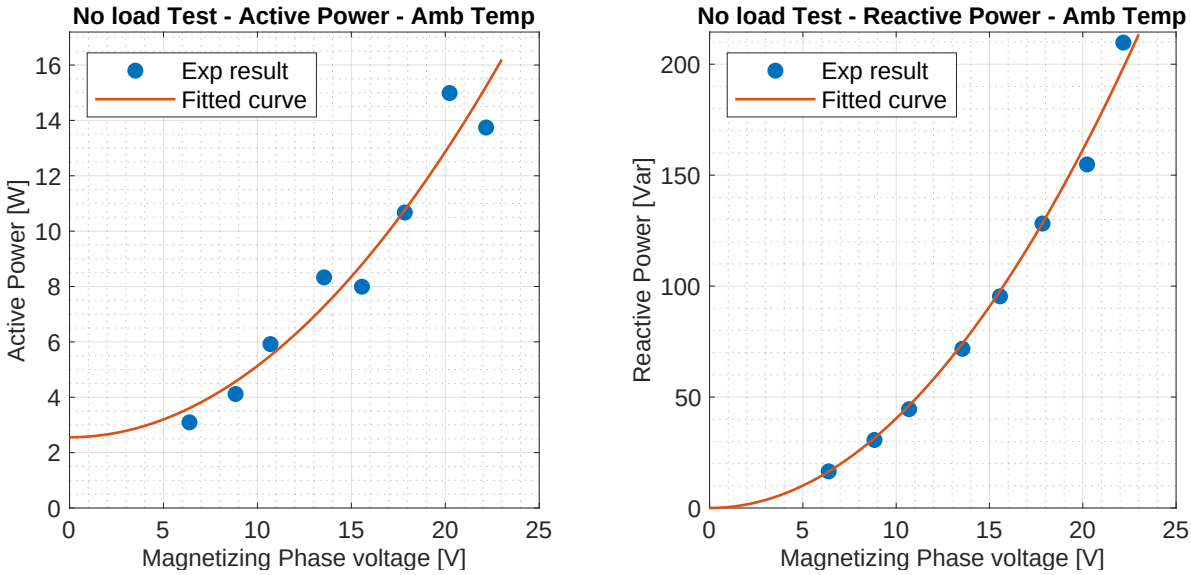

(a) Iron + Mechanical Losses plot

(b) Reactive power plot

Figure 5.2: Ambient no load tests results

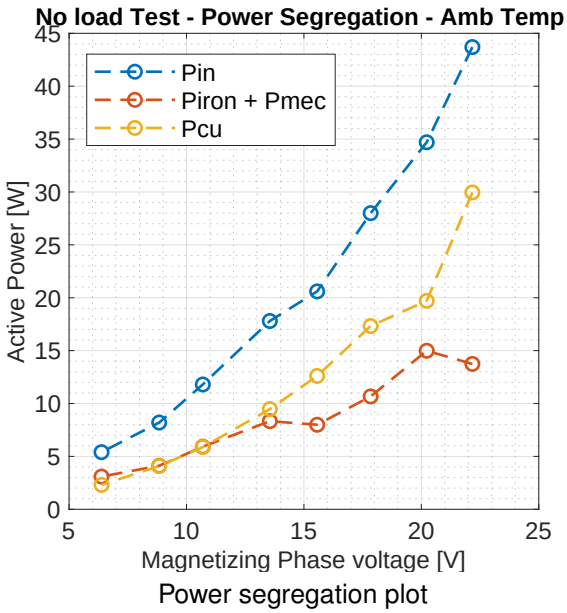

Figure 5.3: Ambient no load tests - Power segregation

An important detail is that, for these tests, the bearings were run in their original state, meaning, still with the manufactures grease, providing lubrication.

With this in mind, and using the previously explained method for the extraction of these parameters, the following results were obtained.

Active Power In figure 5.2 a), the experimentally measured active power excluding copper losses is shown in blue. The decoupling of copper losses P_{cu} from the total active power consumed by the machine is possible due to the fact that the actual stator resistance and current were experimentally measured and thus copper power losses were computed.

Also, and as seen before a quadratic function (in red) with a DC offset is fitted to these measured points ($R^2 = 0.9372$). From this curve and making use of equation (4.7), mechanical power loss P_{mec} and equivalent iron losses resistance R_{Fe} is computed. As expected, for low values of magnetizing voltage $U_m < 5\text{V}$ (and thus stator voltage U_s) the active power consumed by the machine (again, excluding copper losses) is fairly constant and is about 2.55W. This value is assumed to be the maximum value of mechanical losses which accounts to 2.83% of the nominal power of the machine. With this assumption it follows that by removing the, now known, P_{mec} value from the Iron + Mechanical active power, one is left with the Iron losses P_{Fe}. It is now possible to compute the equivalent iron losses resistance R_{Fe}, given by the constant coefficient of this quadratic relation (active power as a function of the square of magnetizing voltage) which yields $R_{Fe} = 116.4\Omega$.

Reactive Power In a similar manner to the previous case, the reactive power curve is analysed, this time making use of equation (4.8). The measured total reactive power consumed by the machine is shown in 5.2 b) in blue. In red, the fitted quadratic curve, obtained in MATLAB is shown. As can be seen the experimental results follow the fitted curve very accurately ($R^2 = 0.9973$). Reactive power increases

quadratically with the magnetizing voltage reaching 209.74Var at nominal voltage and from the fitted curve the value of magnetizing reactance yields $X_m = 7.33\Omega$.

Table 5.1 summarizes the No Load Test results.

Table 5.1: No Load Test Results

	No Load Test - Ambient Temperature
Parameters	
R_{fe}	116.4Ω
X_m	7.33Ω
Power Losses (Peak)	
$\mathrm{P_{mec}}$	$2.55\mathrm{W}$
$\mathrm{P_{Fe}}$	$12.7\mathrm{W}$

5.2.2 Blocked Rotor Test

Following the test procedure previously detailed in section 4 the first ambient temperature blocked rotor tests were performed. The results are shown in figures 5.4 a) and b).

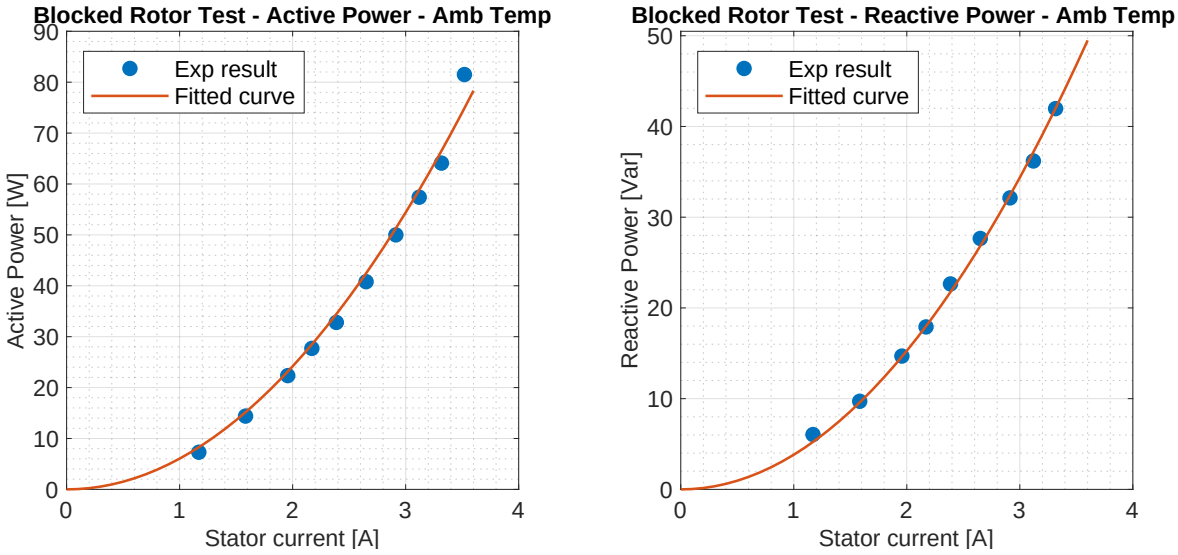

(a)Active Power plot

(b) Reactive power plot

Figure 5.4: Blocked Rotor tests

As described in 4.3.2, the blocked rotor tests were performed under normal operating grid frequency of 50Hz. Also, the input voltage is reduced significantly as to impose the nominal current of 3.66A. An important note must be taken into consideration here. It is assumed that leakage inductances are constant with respect to frequency, meaning that the value obtained in the Blocked Rotor test, where slip is equal to 1, is the same value obtained in the normal operation of the machine, where slip is much smaller than 1. This assumption is backed by the literature [50].

Active Power In figure 5.4 a), experimental active power magnitude data is plotted against the quadratics fitted curve in red ($R^2 = 0.9876$). The data shows that for a stator current average magnitude across the three phases of 3.55A close to the nominal one ($I_{stator} = 3.66\text{A}$), the active power consumed by the machine is 81W. Since the rotor is blocked, and no work is being done, this value of active power consumptions is due to Joule losses in the stator copper windings as well as Joule losses in the rotor caused by the induced currents flowing across the short circuited aluminium cage. As this active power value is the input power to the machine, considering all three phases, there is the need to segregate the stator from the rotor side, the segregation of the stator and rotor losses is done by directly measuring the stator windings resistance. Therefore, the rotor's resistance seen from the stator side, R'_r, can be

calculated using equation 5.1.

$$R'_r = \frac{P_{blockedrotor}}{3I^2_{sRMS}} - R_{smeasured} = 0.914\Omega \tag{5.1}$$

Reactive Power Figure 5.4 b) show the experimentally measured magnitude of reactive power consumed by all of the three phases of the machine plotted against the quadratic fitted curve. The regression is once again coherent with the experimentally obtained data ($R^2 = 0.9973$). Data shows that under nominal stator current and with the rotor blocked there is a consumption of around 46Var of reactive power.

Contrary to the previous case where the stator resistance R_s can be physically measured, in this case it is extremely difficult to directly measure only the stator leakage inductance. The usual procedure is to estimate under some assumptions. One of the most common and simple ones is to consider that the value of leakage reactances of the stator and rotor is the same, meaning that to know either the stator or rotor leakage reactances one uses the total value obtained in the blocked rotor test and making use of equation 4.10, it follows that

$$X_s + X'_r = \frac{Q_{blockedrotor}}{3I^2_{sRMS}} \Leftrightarrow X_s = X'_r = \frac{Q_{blockedrotor}}{6I^2_{sRMS}} = 0.532\Omega \tag{5.2}$$

Table 5.2 contains the extracted parameters from the Blocked Rotor Test.

Table 5.2: Blocked Rotor Test Results

	Blocked Rotor Test - Ambient Temperature
Parameters	
R_s	1.1Ω
R'_r	0.914Ω
X_{ls}	0.532Ω
X'_{lr}	0.532Ω

5.2.3 Load Tests

After the No-Load and Blocked Rotor tests, the computation of the induction machine performance is simulated using the experimentally obtained equivalent circuit parameters. In figure 5.5 are shown the simulated torque-speed and efficiency-speed curves, together with the experimental results for different loads (dotted points).

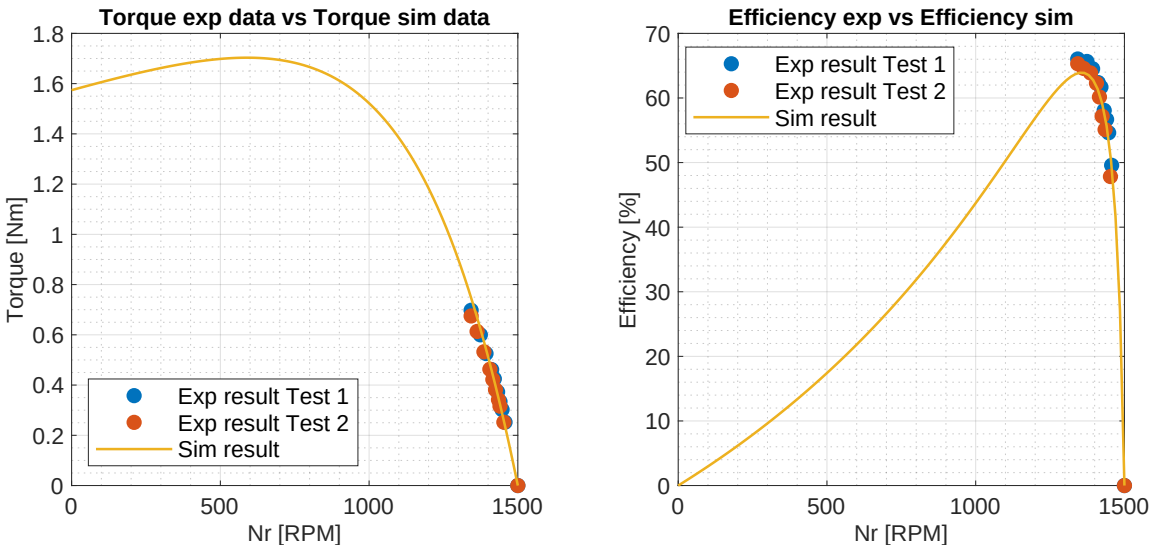

(a)Torque Amb Temperature (b)Efficiency Amb Temperature

Figure 5.5: Ambient Load tests

For these first Load tests, the first experimental setup was used, and as explained in chapter 4 the induction machine is tested by coupling its rotor shaft to the small 240W DC machine acting as a generator. The DC generator is then connected to a rheostat acting as a pure resistive load.

Figure 5.5 a) and b) shows that the obtained experimental results follow the simulated curves as expected, although not perfectly. The obtained differences between the experimental data (dotted data) and the simulation, that results in a 2.03% error, comes from mainly two sources. The first is the fact that the conductors, both stator and rotor ones, may be at a higher temperature than that used for the simulations, in which the ambient temperature measured in the lab at the time of the tests was used. The temperature of the conductors was not measured, and although the cooling fan was used, it's not possible to know this for sure. The other one is the fact that throughout the test, the input voltage was constantly being regulated due to the internal voltage drop in the motor this made maintaining a constant nominal input voltage difficult.

5.3 Cryogenic Temperature Test Results

With the machines ambient temperature operation analysed, cryogenic tests followed. As explained in chapter 4 the operation of the machine submerged in liquid nitrogen requires some preparation. The first step was determined to be the removal of the cooling fan. This step is rather important and can be easily overlooked. There are two main problems with the cooling fan, both mechanical problems. The first is that this fan is made out of a common polymer used in normal operating conditions, the specific polymer is unknown but it's mechanical properties are not guaranteed to be compatible with extreme temperatures operation (very high or very low temperatures).The second is the fact that the cooling fan may introduced unwanted turbulence in the LN_2. Figure 5.6 shows an image of the IM taken after a cryogenic load test.

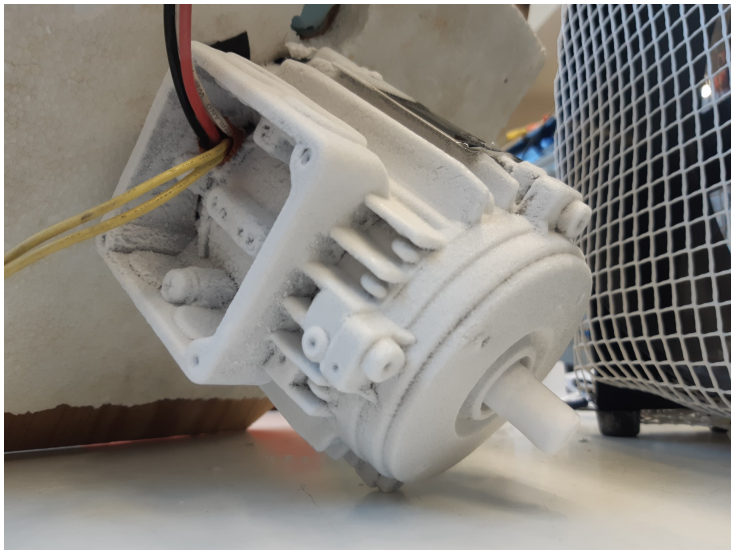

Figure 5.6: IM after LN2 bath

The phenomena of material properties change as a function of strain and temperature is modeled by Hooke's law [51], the analysis of this phenomena is outside the scoop of this thesis. Nonetheless a simple explanation can be useful.

Different materials have a very wide range of behavior when subject to an applied mechanical load. Generally materials can be ductile where an increase of load (strain) applied to a material is followed by a relatively small change in stress, i.e force per unit area, can also be brittle where an increase of load applied is followed by a large increase in stress, or a mixture of the two (plastic behavior). When a load is applied to a ductile material, as the load increases, the material deforms, effectively distributing the load across the material, this deformation in polymers is usually reversible when the load decreases to 0, and the material restores its original shape (elastomers). When the load is applied to a brittle material, it does not deform (load is localized), stress increases until it causes a failure.

The issue with this is that a seemingly plastic material, as the one used for the cooling fan, is so for a specific range of temperatures, in fact, most polymers are plastic for ambient temperatures but extremely brittle in very low temperatures as can be seen in the figure 5.7 [52] where a temperature dependent

Stress vs Strain plot for the common polymer PET is shown:

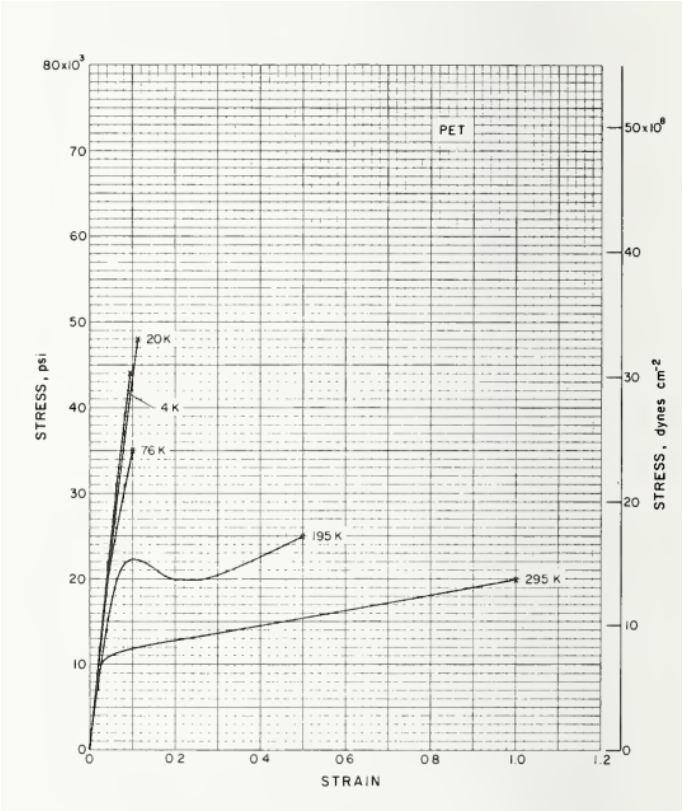

Figure 5.7: Stress vs Strain plot of PET for different temperatures [52]

This brittle behavior in liquid nitrogen added to the fact that the fan would introduce additional turbulence to the liquid nitrogen, led to the removal of the fan. It is also important to stress that this same ductile to brittle transition analysis can be made for the structural and conductor metals of the machine. Research has shown that while face centered cubic lattice (FCC) based metals like aluminium and copper do not experience a ductile-brittel transition for temperatures higher or around liquid nitrogen temperature of -196ºC, this is not true for body centered cubic lattice (BCC) based materials like iron. This effect tho, greatly varies with the alloy and impurities content. With FeSi alloys demonstrating to be very stable under these conditions.

5.3.1 No-Load Test

Cryogenic No-Load tests follow the same procedure as in Ambient temperature operation explained in chapter 4, with a few added difficulties. These difficulties were related to the cryogenic environment it self, which most have already been described in previous chapter 4. The most crucial one to the No-Load test is the ice build up on the shaft coupler, which makes the measurement of rotor angular velocity using the optical tachometer, almost impossible. This process takes some time though, around 6 minutes in average across all the tests performed is the time it takes for the ice buildup to be enough to render the tachometer useless. By the 9 minute mark after liquid nitrogen is poured into the cryostat, the coupler, shaft and support screw bars are fully frozen. Figure 5.8 is an image taken after 10 min of

operation in no load condition and after trying to remove most of the ice from the area, by hand, using protective gloves.

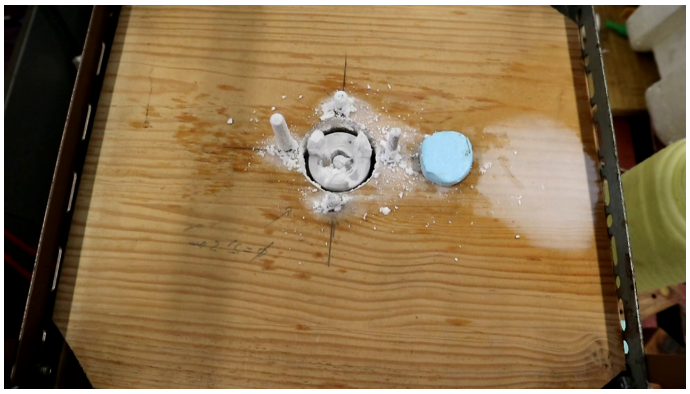

Figure 5.8: Frozen coupler and surroundings

Figures 5.9 and 5.10 show the No-Load test results for cryogenic operation.

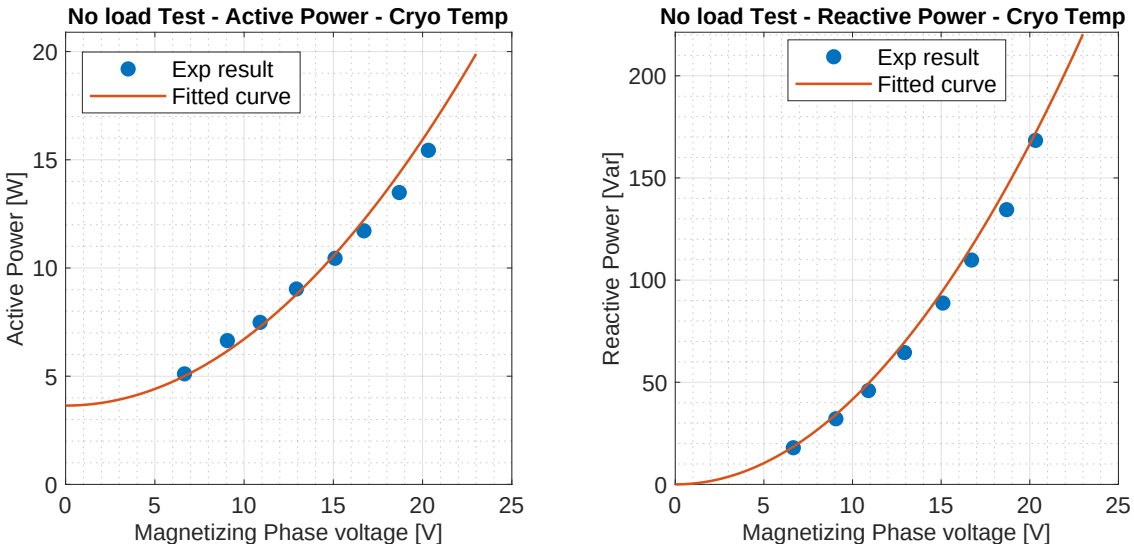

(a) Iron + Mechanical Losses plot

(b) Reactive power plot

Figure 5.9: No load tests cryogenic

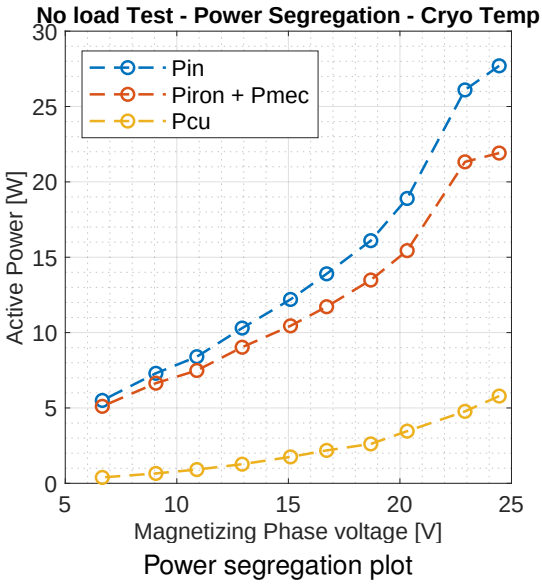

Figure 5.10: No load Power Segregation Cryogenic

Active Power Figure 5.9 a) shows, in blue, the experimentally measured active power, excluding copper losses, for the No-Load cryogenic tests, measured at the input of the induction motor stator. In red is shown the quadratic theoretical curve obtained by fitting the theoretical function explained previously, to the experimental data as in the ambient temperature case. As observed, the results are coherent with the expected behavior from this test, and correlation between the theoretical curve and the measurements is very good ($R^2 = 0.985$). The same analysis made for the ambient temperature case is done here. From the fitted curve the obtained maximum value of mechanical power losses is $P_{mec} = 3.64\text{W}$. Furthermore maximum iron power losses value was also computed , with the value of $P_{Fe} = 15.1\text{W}$. With this, the equivalent iron losses resistance parameter computation follows, with a final result of $R_{Fe} = 97.6\Omega$

Reactive Power Figure 5.9 b) shows the experimentally obtained reactive power data in blue, as well as the quadratic fitted curve in red. The results are coherent with the expected behavior, with the experimental data following the fitted curve very well ($R^2 = 0.993$). Maximum reactive power consumed by the induction motor in this test was 222.86Var, at nominal stator voltage. Furthermore, from the analytical fitted curve magnetizing reactance was computed, the result is a value of $X_m = 6.97\Omega$

Table 5.3 summarizes the obtained results from the No-Load test at cryogenic temperature.

Table 5.3: Cryogenic No Load Test Results

No Load Test - Cryogenic Temperature	
Parameters	
R_{fe}	97.6Ω
X_m	6.97Ω
Power Losses (Peak)	
$\mathrm{P_{mec}}$	3.64W
$\mathrm{P_{Fe}}$	15.1W

5.3.2 Blocked Rotor Test

After the No-Load Test, a series of Blocked Rotor tests were performed. These tests follow the same procedure as in the ambient temperature operation, and the same precautions highlighted for the cryogenic tests are followed here. The fact that heat can be extracted from the machine fairly quickly grants an opportunity of going beyond the nominal current in this test, this is not possible in ambient temperature operation, as the machine to air heat transfer flux is insufficient to maintain a temperature where the integrity of the machine's material is guaranteed. This opportunity might give an insight into some problems and effects that may happen to the machine in this environment, when currents go far beyond the nominal ones, as in motor startup. The obtained results are shown in figure 5.11.

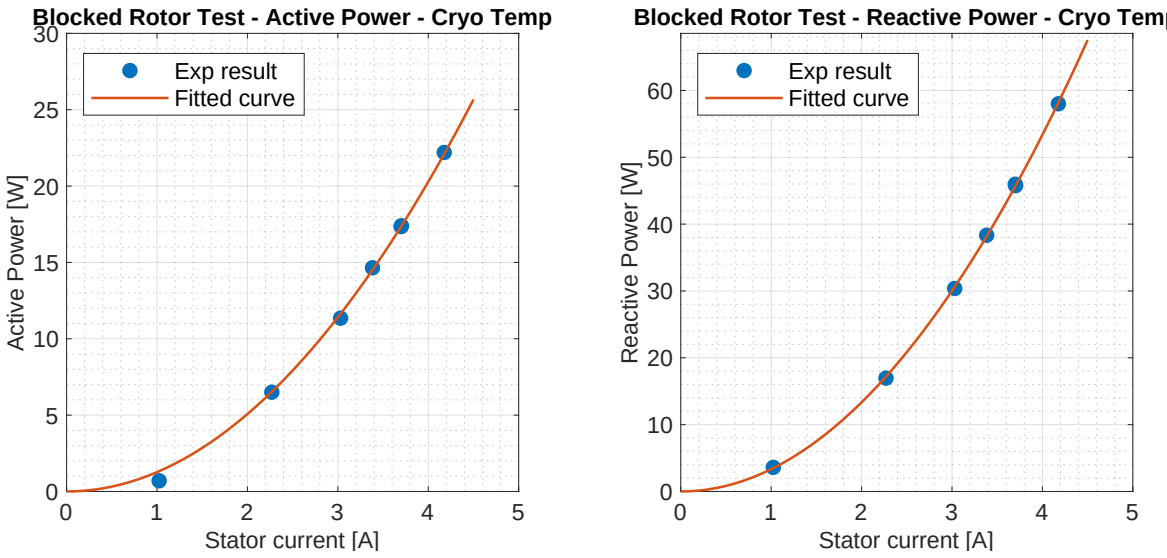

(a)Active Power plot

(b) Reactive power plot

Figure 5.11: Blocked Rotor tests Cryogenic

Active Power Figure 5.11 a) shows the consumed active power, in blue, as a function of the stator current, measured in this test. In red the obtained fitted curve, closely follows the experimental results, the results are thus coherent with the expected behavior ($R^2 = 0.9984$). As explained before, maximum stator current in this test is above the nominal current, with a value of 4.18A it is 14.21% above the nominal (ambient temperature) one. Despite this no unexpected behavior is shown in the measured data, its clear that even for this larger currents, the analytical curve fully models active power consumption. Maximum active power reached in this test is 22.20W, with this information and using the measured stator resistance at 77K (-196ºC), with a value of 0.2Ω, the obtained rotor resistance is computed to be $R'_r = 0.223\Omega$

Reactive Power Seen in figure 5.11 b) is the measured reactive power during the test (in blue). Once again the results are coherent with the analytical expected results ($R^2 = 0.9999$), shown in red as the

computed fitted curve. Just as in the measured active power, no unexpected behavior is shown in the data for currents up to 14.21% above the nominal ones, thus magnetic leakage losses do not appear to be affected by the cryogenic temperatures. In the same manner as previously noted, leakage reactance parameters were computed, the obtained stator and rotor leakage reactances are shown in table 5.4, summarizing all of the obtained results in the Blocked Rotor Tests.

Table 5.4: Blocked Rotor Test Results

	Blocked Rotor Test - Cryogenic Temperature
Parameters	
R_s	0.2Ω
R'_r	0.223Ω
X_{ls}	0.556Ω
X'_{lr}	0.556Ω

5.3.3 Load Tests

In this subsection, the cryogenic temperature load tests are shown. Cryogenic tests were performed using both experimental setups described in section 4.1, the first tests were performed using the first experimental setup for its easiness of assemble and use. Later tests were performed using the second experimental setup to be able to test the machine close to its maximum torque.

Following the Load tests procedure as before, the test started after thermal equilibrium was reached, confirmed by the stator phase winding resistance. An analytical approach was used to estimate the stator winding resistance, using the well known one term linear relation between the resistivity of a material and its temperature, shown in chapter 3.

Figure 5.12 shows Torque vs Speed and Efficiency vs Speed curves for three sets of experiments ranging from low load tests up to maximum load tests.

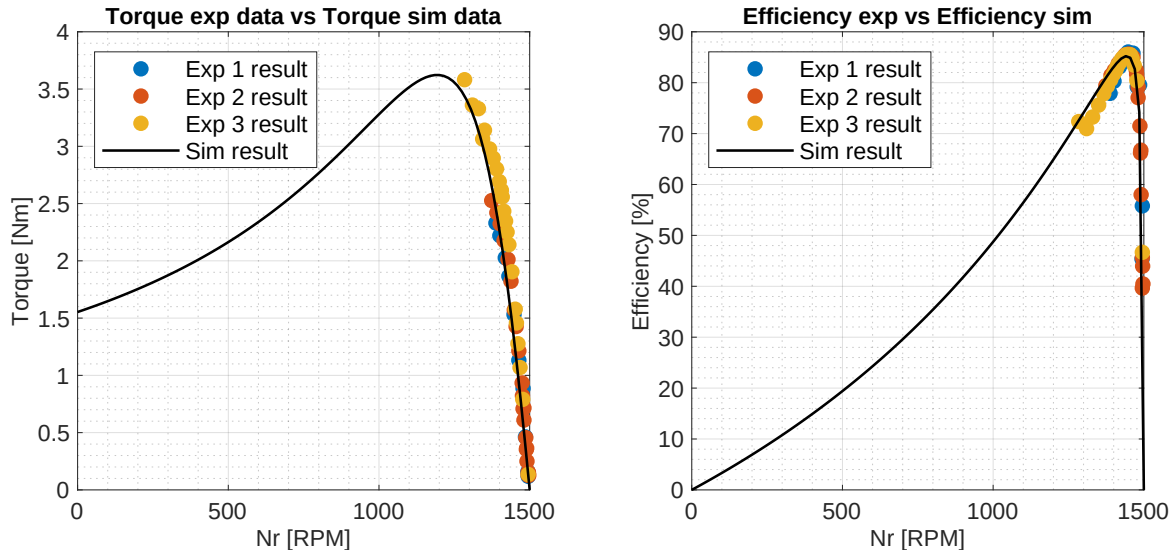

(a)Torque Cryo Temperature (b)Efficiency Cryo Temperature

Figure 5.12: Load tests

In addition, table 5.5 summarizes the main results from the cryogenic load tests.

Table 5.5: Final Cryogenic Tests Results

Final Load Tests Results - Cryogenic Temperature	
Parameters	
Torque(@Peak Efficiency)	1.95 Nm
Peak Torque	3.58 Nm (@ $\eta = 72.4\%$)
Pmec (@Peak efficiency)	294.3 W
Peak Pmec	481.57 W (@ $\eta = 72.4\%$)
Peak efficiency	85.2%
Peak Stator Current	15.14A

The objective of the first two tests was to assert the smooth running of the machine and setup, making sure that everything would behave as expected, with the machine current limited to its nominal values. During these tests the machine remained very stable, and no issues were detected apart from the loud noise coming from the induction motor's bearings, which was expected since no grease was present in them, metal to metal contact was therefore a constant with the only lubrication being provided by the liquid nitrogen itself.

Experiments proceeded and by the third test, at an average stator current of 5.8A across all three phases and 280W of input power, the nominal 240W output power of the DC generator was achieved. It was apparent that the first experimental setup would not suffice, it was in this light that the second experimental setup was built. The new 1kW nominal power DC generator was chosen as to be able to meet the new load demands.

With the second set up built, a new objective was set. The objective of this tests was to try to reach the maximum torque and efficiency of the induction motor as computed in the simulation. Furthermore an attempt to go beyond the maximum torque point was to be made, this was important to verify if there was an unexpected phenomena in this region of operation. In addition, it was also relevant at this stage to get data from speeds lower than the maximum efficiency point, this is important to analyse the efficiency drop behavior after the maximum point.

It is important to note that this phase of tests was limited to the measuring equipment maximum ratings though. Indeed the measuring wattimeters used had a maximum current rating of 10A, and according to the simulations this was not enough to reach the desirable maximum torque of the machine, which was computed to be reached at a stator current magnitude of 15A. Nonetheless this didn't hinder the tests in any way and the machine's behavior continued to be stable and smooth with no out of the ordinary sounds, measured values or mechanical oscillations.

In the last cryogenic tests a new wattimeter circuit able to measure currents bigger than 10A was built. For this, voltage and current transducers as well as a Data Acquisition System was used, the final circuit is shown in figure 4.7. After testing the wattimeter circuit and evaluate its precision, with good results, the full load tests proceeded.

During these last set of tests the machine run remarkably smooth even for very high loads, despite the sometimes high pitch sound coming from the bearings. It is difficult to know for sure the cause of the high pitch sound that sometimes appeared during high loads, but three possibilities are the most likely. The first is the fact that the bearings used were chosen by the manufacture, amongst other reasons, for a specific maximum load torque applied to the machine's shaft, which could be surpassed in the cryogenic tests.

Furthermore, the difficulty of precisely align the IM and DC generators shaft in this vertical setup might contribute to this sound also.

The third possibility is the fact that this sound is not really an anomaly in this cryogenic environment, meaning that the presence of liquid nitrogen inside the bearings, which at lower loads acts as a lubricant, might be the cause of the sound. Here it is important to note that the loads acting on the bearing can be enough to change the phase of nitrogen present inside it, if this happens the presence of pockets of

nitrogen gas will cause excess friction and thus the sound.

Regarding the obtained results themselves, they were aligned with the expected. The maximum stator current reached in this tests was short of 16A, at an average stator current of 15.14A(RMS) across the three phases, a maximum of 399.152W of active power at the load was reached. This was achieved at an active IM input power of 665.5W with 72.4 % efficiency and at 1284RPM rotor speed, so 84RPM short of the maximum load torque, according to the simulations. This maximum torque was not possible to reach though, despite a few attempts, this was due to, the expected, instability of this region of operation. Nonetheless, a peak torque of 3.58Nm was measured at 1284RPM. Furthermore, both torque and efficiency measured data follow the simulated results very well, even in the descent portion of the efficiency curves witch was an important question in the beginning of the tests. Also the predicted maximum efficiency point was in this case also confirmed to be 85.2% at 1441RPM.

5.3.4 Load Tests - 1h stability Test

A natural progression when analyzing the performance of a cryogenic machine is to evaluate its stability of operation. This point is the focus of the next subsection of this thesis.

The tests performed up until this point were quite short, around 15 to 20 min of constant machine operation. This is clearly not enough for a complete understanding of the machine stability, nor it is a realistic operation time. It is then vital to test long duration operation. At first this test seems rather simple to do and one might thing that the best thing to do was to leave the machine running for, say 6 hours or more. While this is an ideal solution it is not a realistic one for a few reasons. As explained before there is no active cooling solution applied to the IM in this thesis, liquid nitrogen is poured into the LN_2 container by hand and after the heat transfer process, the resultant nitrogen gas is vented to the atmosphere, whether it is through the necessary venting hole or the unwanted, loss producing, small gaps between the LN_2 container wall and lid. This means that throughout all the performed tests the LN_2 container's liquid nitrogen levels was constantly checked and the necessary liquid nitrogen added, this was done on average every 5 min of operation. Also at any time the maximum volume of liquid nitrogen stored in the lab was 40L. These 40L, obviously, had to be enough for every experiment planned in the laboratory for that period of time, multiple parallel experiments were being made and due to the nature of cryogenic experiments, a lot needs to be used. Most of the liquid nitrogen consumption occurs in the cooling down process, and it takes a good fraction of these 40L to cool down the machine to 77K.

The decision was made to limit the long duration test to 1h. During this period the IM was to be operated under a current of 3.66A, meaning a mechanical power of $P_{mechanical} \approx 90W$, close to the one obtained in ambient temperature tests.

Figure 5.13 a) and b), shows the average root mean square value of stator current and total input active power, respectively, across the duration of the test.

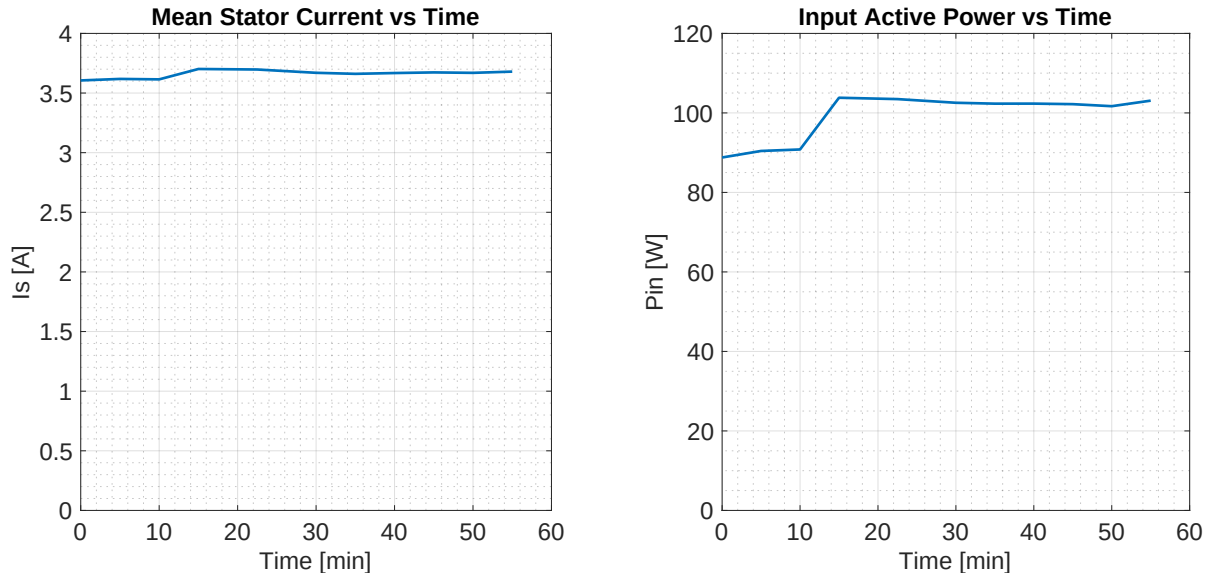

(a) mean stator current during test

(b)Input power during test

Figure 5.13: Stability test results

The first thing to note is the apparent increase of power from the 10min mark up to the 15min mark, visible in both plots but more so in the input power plot. This increase in power is actually not due to any electric phenomena but rather a mechanically induced increase in load. During the first minutes of the test there was an obvious mechanical oscillation in the structure, caused by the IM wood support that was not properly fixed to the rest of the structure. Therefore in an attempt to get rid of this oscillations, the wood support was rotated and properly secured to the structure, causing an increase of mechanical load of the induction machine. Despite this small issue, the machine remained stable throughout test, no unexpected behaviour was identified both in the measured data and the observation of the test itself. A maximum of 2.1W variation was present in the input power data, that is 2.02% of the machine's steady state input power of 103.8W after the 15min mark. The machine's cryogenic operation is therefore stable.

5.4 Results Discussion

In this section the obtained experimental results from ambient and cryogenic operation are discussed. First, the impact of the cryogenic operation in the equivalent circuit's parameters is analysed, followed by the torque and efficiency results. In addition, the difference of mechanical, iron and copper losses are analysed to fully characterize and summarize the findings in this thesis.

Table 5.6 shows the obtained results concerning the equivalent circuit parameters. Starting with the stator resistance, data shows a reduction of 81.8% of its value, this is inline with the expected reduction according to the linear resistivity as a function of temperature equation shown in chapter 3. This reduction is apparent in figure 5.14 where the blocked rotor test active power as a function of stator current is shown. Here as can be seen for a stator current of 3.7A, close to the nominal one of 3.66A, the active power consumed in ambient temperature is around 81W while in cryogenic temperature (77K) is around 17W. This significant reduction in stator conductor resistance translates into a relative difference of -35% in the peak stator copper losses as shown in table 5.7.

Table 5.6: Equivalent circuit parameters results

Parameters	Ambient Temperature (T = 20ºC)	Cryogenic Temperature (T = -196ºC)	Difference
R_s	$1.1\,\Omega$	$0.2\,\Omega$	$-81.8\,\%$
$R_{r'}$	$0.914\,\Omega$	$0.223\,\Omega$	$-75.6\,\%$
R_{Fe}	$116.4\,\Omega$	$97.6\,\Omega$	$-16.1\,\%$
X_m	$7.33\,\Omega$	$6.97\,\Omega$	$-4.9\,\%$
X_{ls}	$0.532\,\Omega$	$0.556\,\Omega$	$+4.5\,\%$
$X_{lr'}$	$0.532\,\Omega$	$0.556\,\Omega$	$+4.5\,\%$

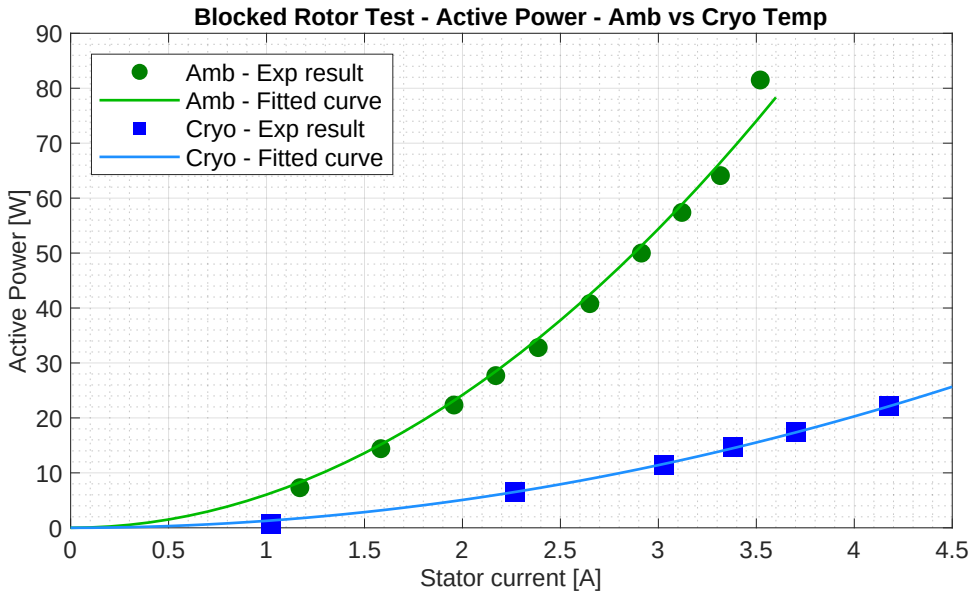

Figure 5.14: Amb vs Cryo Blocked Rotor - Active Power

The rotor resistance R'_r follows a similar reduction of 75.6%. This is lower than the reduction seen in the stator copper windings resistance because the rotor bars are made of aluminium. In particular

the resistivity of the aluminium alloy used in this rotor, Al2024(O), is highly non linear in this region of temperatures, starting to plateau at around 100K. This means that the reduction in the aluminium rotor bars resistance is lower than that of an equally sized copper bars rotor. Note that this fact is rather important as reducing the rotor resistance has the unwanted effect of lowering the machine's starting torque, this effect can be seen in figure 5.18, where the simulated starting torque in cryogenic temperature is actually lower than that in the ambient temperature case. In extreme cases this reduction could mean that the induction motor does not produce enough torque to start, although this is not the case.

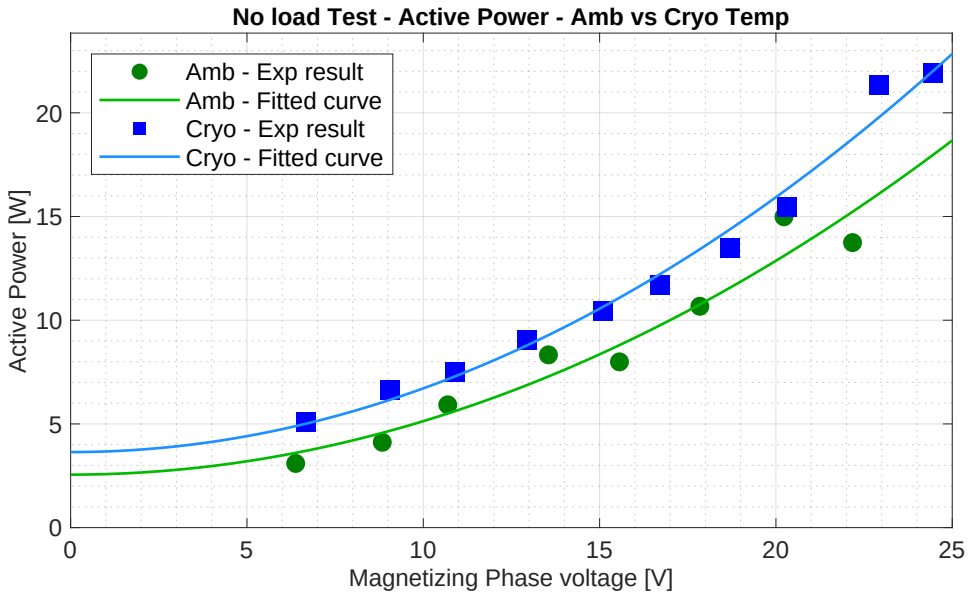

Figure 5.15: Amb vs Cryo No Load - Active Power

Regarding the equivalent iron losses resistance R_{Fe}, it also presents a reduction in its value, this time a reduction of 16.1%. This is an expected change as seen in [37] [40]. Since this reduction in temperature causes an increase in the iron core lamination's conductivity, it follows that eddy currents should also increase, causing an increase in iron losses. This is seen in table 5.7 where an increase of 19.3% in the the iron losses is noted. Furthermore it seems that an increase of 16.1% in the equivalent iron losses resistance would mean an equal increase in the iron losses, witch is not the case, as iron losses increase is 3.2% higher. This is most likely due to an increase in hysteresis losses, as the voltage drop at the stator resistance is lower, leading to a higher magnetization voltage (higher magnetic flux density). Hysteresis losses are also temperature dependent, but its change with temperature is very much material depended [53].

Table 5.6 also shows that the magnetizing reactance X_m had a relative reduction of 4.9%. In absolute terms it is a difference of 0.36Ω. This can be observed in figure 5.16 as the difference of reactive power increases for higher values of magnetization. As the magnetizing reactance represents the magnetic energy required to create the rotating magnetic field, the influence of the temperature on it should be minimal. This error of 4.9% is very small and may also be originated due to slightly different stator voltages, between the ambient temperature and cryogenic operations (the level of saturation between

machines can be slightly different).

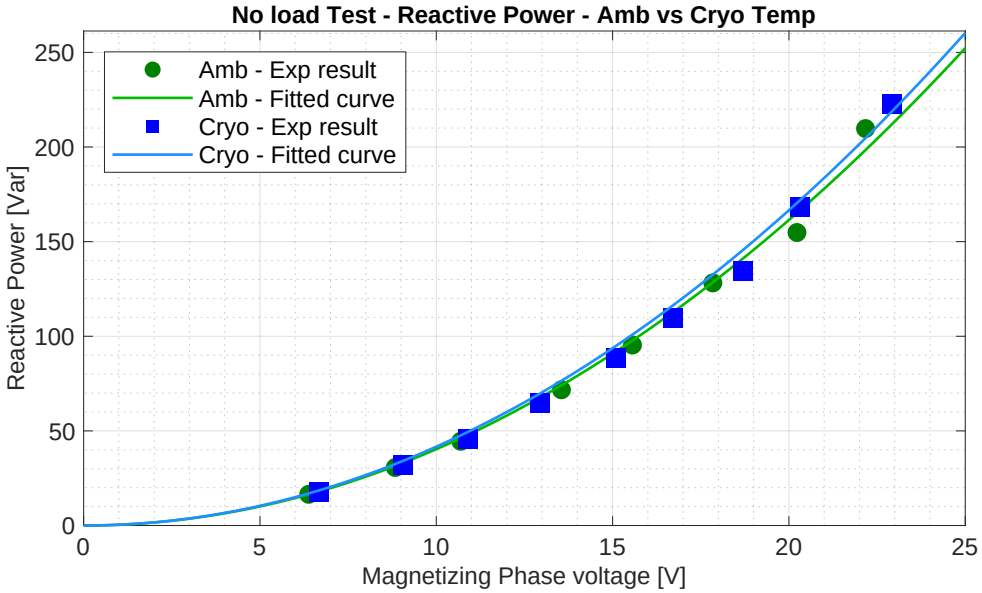

Figure 5.16: Amb vs Cryo No Load - Reactive Power

A similar case to the previous magnetizing reactance one, can be made for the leakage reactances X_{ls} and X'_{lr}. These had a relative increase of 4.5% as seen in table 5.6, in absolute terms an effective increase of 0.024Ω. This difference is also observed in figure 5.17, just as before, as the difference of reactive power increases for higher values of magnetization. As these reluctances represent the magnetic flux leakage losses, which are dependent on the machines geometry, this increase is not representative of a physical change in the machine's magnetic or electric quantities and, therefore, may be related to measurement errors or an increase level of saturation in the iron core.

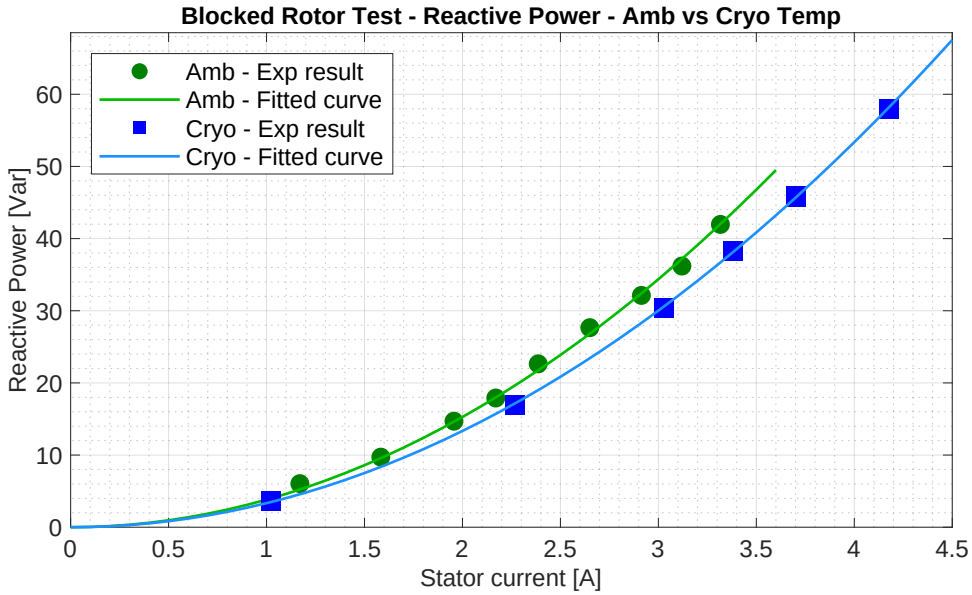

Figure 5.17: Amb vs Cryo Blocked Rotor - Reactive Power

Table 5.7 shows six features of merit used to compare the induction motor performance, in cryogenic

temperature with the ambient temperature baseline, as an electro-mechanical system.

Table 5.7: Features of Merit results

	Ambient Temperature (T = 20ºC)	**Cryogenic Temperature (T = -196ºC)**	**Difference**
Torque (@Peak η)	$0.72\ \mathrm{Nm}$	$1.95\ \mathrm{Nm}$	$+170.8\ \%$
Mechanical Power (@Peak η)	$101.9\ \mathrm{W}$	$294.3\ \mathrm{W}$	$+188.52\ \%$
Mechanical Losses	$2.55\ \mathrm{W}$	$3.64\ \mathrm{W}$	$+42.8\ \%$
Iron Losses (Peak)	$12.7\ \mathrm{W}$	$15.1\ \mathrm{W}$	$+19.3\ \%$
Stator Copper Losses (Peak)	$35.9\ \mathrm{W}$	$23.35\ \mathrm{W}$	$-35\ \%$
Efficiency (Peak)	$63.9\ \%(@s = 0.1)$	$85.2\ \%(@s = 0.04)$	$+33.3\ \%$

Starting with mechanical losses, a relative increase of 42.8% is shown, from 2.55W in ambient temperature to 3.64W in cryogenic temperature, this can be clearly seen in figure 5.15. This increase is expected because, as discussed before, in the cryogenic temperature tests the machines bearings were operated without lubricating grease, with the lubrication being provided only by the liquid nitrogen itself, which is not an effective lubricant as explored before.

Regarding torque, it shows that the torque at peak efficiency had a relative increase of 170.8%, going from 0.72Nm in the ambient temperature regime to 1.95Nm in cryogenic operation. Furthermore figure 5.18 shows the Torque vs Speed simulated curves as well as measured experimental data for both cases. Here it is clear the overall increase in torque in cryogenic operation compared to the ambient temperature case, most notably the increase in peak torque, that had a value, according to the simulated results, of around 1.7Nm in ambient temperature and around 3.62Nm in cryogenic temperature, with a maximum measured torque during testing of 3.58Nm, 2.1 times higher than the ambient temperature peak torque possible. It is also worth mentioning that the machine could operate without thermal restraints until around 3.58Nm, as the $\mathrm{LN_2}$ had enough capacity to remove all produced losses, without an increase of temperature.

Mechanical power also saw a considerable increase at peak efficiency with a value of 101.9W in ambient temperature operation compared to 294.3W in cryogenic operation, a relative increase of 188.52%. This is expected with the increase of efficiency, that is going to be discussed in the next paragraph, because as the electric to mechanical energy conversion is done more efficiently, it follows that mechanical power at the rotor shaft must increase, as seen before with the increase in mechanical torque discussed in the previous paragraph.

It is also worth mentioning that a peak mechanical power of 481.57 W was achieve. This point of operation was thermally stable, as the $\mathrm{LN_2}$ had enough capacity to remove the heat produced by the machine. This could virtually mean that the same induction machine can operate until this maximum power, resulting an relative increase of 372.59% when compared with the 101.9W at ambient temperature.

Finally regarding efficiency, table 5.7 shows that while in ambient temperature peak efficiency was 63.9%, in cryogenic temperature it increased to 85.2% an absolute increase of 21.3%. This was ex-

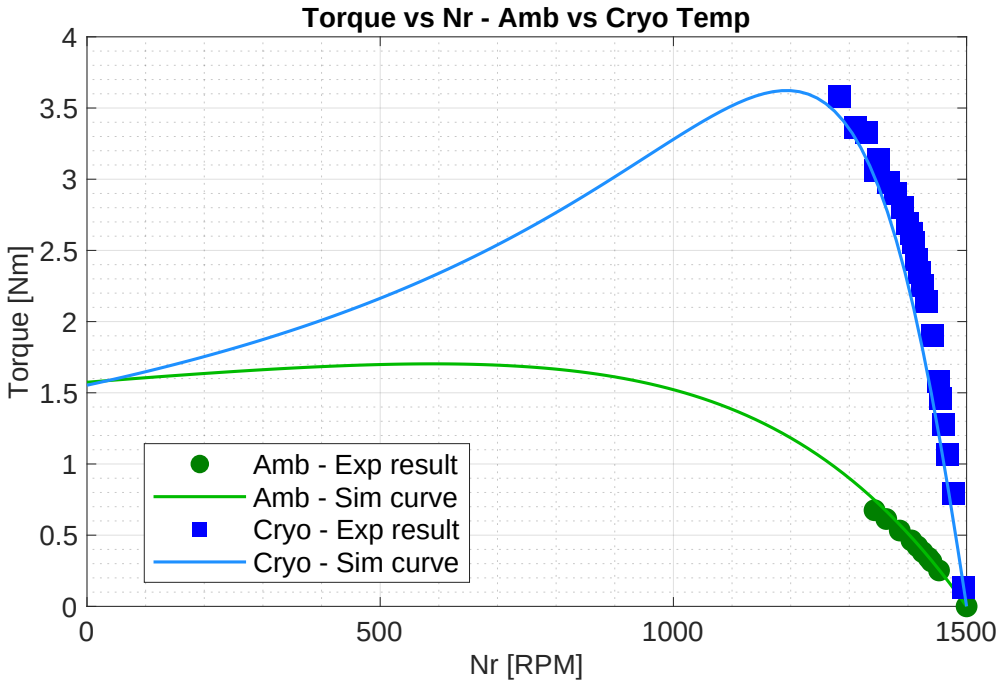

Figure 5.18: Amb vs Cryo Torque

pected according to the simulated curves in figure 5.19, nonetheless a surprising result. Also while peak efficiency in ambient temperature was at around 1350RPM rotor speed, in cryogenic temperature this maximum value was measured at around 1440RPM. Nominal point is therefore shifted 90RPM to a higher speed, getting close to the 1500RPM synchronous speed of the rotating field.

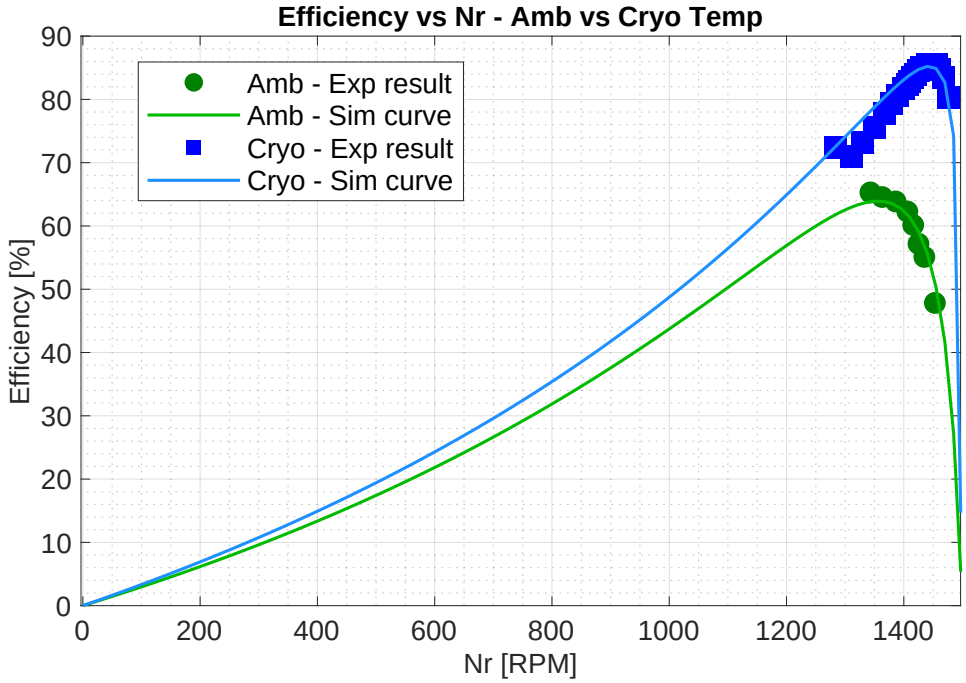

Figure 5.19: Amb vs Cryo Efficiency

Chapter 6

Conclusions

In this thesis the performance of a conventional air-cooled induction motor submerged in liquid nitrogen was analysed by comparing it to its ambient temperature performance. For this purpose, both temperature and skin effect significant influence on the magnetic and electrical properties of the motor materials were analysed. Furthermore, the impact of cryogenic conditions on the overall performance and on the equivalent electric circuit parameters were analyzed.

To validate impact of cryogenic conditions on the performance of the induction machine, experimental setups was developed to test a 90W induction machine submerged in liquid nitrogen. Moreover, a methodology for the preparation and study of a conventional induction motor submerged in a liquid nitrogen(-196ºC) environment was purposed. The used models and proposed methodology were compared with the obtained experimental data and validated.

The impact of the cryogenic cooling on the reduction of the equivalent circuit resistances has shown to be equal to the expected reduction based on the proposed analytical models. Also, the obtained results are in line with the literature regarding the geometry dependent leakage and magnetizing reactants which show a negligible change in normal operation of the motor.

Regarding the motor's overall performance and losses, the results indicate significant advantages in the motor operation in cryogenic temperatures. Despite a small increase of mechanical losses (1.1W), expected in liquid nitrogen operation, and, the confirmed, 19.3% increase in iron losses due to increase conductivity of the iron core, the significant 35% decrease in joule losses result in an absolute increase of 21.3% in efficiency, from 63.9% to 85.2% a considerable number even for low power machines.

This efficiency improvement in the electromagnetic to mechanical power conversion, results in an increase of 170.8% in torque and a 188.5% in mechanical power at peak efficiency, showing that significant improvements in power and torque densities can be made when operating an induction motor in very low temperatures.

These results have remarkable consequences in applications where high power and low weight is needed, as it is the case of aircraft and aerospace platforms which not only are extremely weight dependent but also have ,in current designs, the access or the ability to use cryogenic fluids in their systems, as liquid hydrogen. Furthermore, current platforms such as military and commercial ships,

that, in the last decades, have made considerable investments both on fleet electrification and the use of HTS electric motors, can have in cryogenic cooled induction motors, a lower cost, less complex and more reliable alternative, with scientifically well founded results.

6.1 Future Work

In this thesis a passive cooling solution was used. This solution is impractical in real applications, both from a nitrogen consumption and long term reliability point of view. An active cooling solution must be analysed and nitrogen consumption measured. In addition, from a system point of view the efficiency of the chosen thermal management system must be included in the cryogenic motor + cooling analysis, and an efficiency value for the system as a whole considered.

This analysis must also include an economic viability study, tailored to the specific application where this kind of drive solution is to be installed, despite the already positive general consensus of this type of design viability.

Finally, even though the change in leakage and magnetizing reactances is measurably small and generally considered negligible in the current literature, further work must be done to ensure a complete understanding of the phenomena, especially for applications that use hydrogen or any cryogenic fluid below nitrogen temperatures.

Also, transient and high magnetic loading operation must be explored, as these regimes have largely been under studied and its consequences have particular effects even in ambient temperature operation.

Bibliography

[1] G. Ferraris. Electrodynamic rotation by means of alternating currents. In *Opere di Galileo Ferraris*, volume 1, pages 333–348. Ulrico Hoepli Editore, 1902.

[2] N. Tesla. A new system of alternate current motors and transformers. *Proceedings of the IEEE*, 72 (2):165–173, Feb. 1984. doi: 10.1109/PROC.1984.12838.

[3] M. Dolivo-Dobrovolsky. Aus der geschichte des drehstroms. *ETZ Elektrotechnische Zeitschrift*, (26–29):341–344,354–357,366–369,376–377, 1917.

[4] A. T. de Almeida, F. J. T. E. Ferreira, J. Fong, and P. Fonseca. Eup lot 11 motors, final report. ISR-University of Coimbra, 2007.

[5] M. Kostic. Effects of voltage quality on induction motor's efficient energy usage. In *Induction Motors - Modelling and Control*. Prof. Rui Esteves Araújo,IntechOpen, November 2012. doi: 10.5772/51223.

[6] C. of European Union. Commission regulation (eu) 2019/1781. *Official Journal of the European Union*, pages 74–94, 2019.

[7] J. G. Bednorz and K. A. Müller. Possible high tc superconductivity in the ba-la-cu-o system. *Zeitschrift für Physik B Condensed Matter*, 64:189–193, June 1986. doi:10.1007/BF01303701.

[8] J. H. Redmond and F. W. Bott. Development of cryogenic electric motors. *SAE Transactions*, 72: 257–268, 1964.

[9] S. Claudet. Introduction to cryogenics for accelerators. `https://https://indico.cern.ch/event/565314/contributions/2285754/attachments/1472534/2279197/CAS_Sweden_Cryo_2017_sc.pdf`, June 2017.

[10] R. Fast. Development of a large centrifugal cryogenic pump. In *Advances in Cryogenic Engineering*, volume 37, pages 845–851. Plenum Press, 1992.

[11] M. Tomsic. Cryo-thermal management of high power density motors and drives. `https://https://arpa-e.energy.gov/sites/default/files/2021-03/10_Hyper%20Tech%20ARPA-E%20ASCEND%20Slide%20Presentation-kickoff%20meeting%20Final_pdf.pdf`, January 2021.

[12] C. Ai, Y. Huang, and H. Wang. Coupled electromagnetic and thermal analysis of a 15kw cryogenic induction motor for submerged liquefied natural gas pumps. In *2020 23rd International Conference on Electrical Machines and Systems (ICEMS)*, pages 745–748, December 2020. doi:10.23919/ICEMS50442.2020.9290937.

[13] R.Shively. Submerged cryogenic motor materials development. *IEEE Electrical Insulation Magazine*, 19(3):7–11, June 2003. doi:10.1109/MEI.2003.1203016.

[14] S.Rush and L.Hall. Tutorial on cryogenic submerged electric motor pumps. In *Turbomachinery and Pump Symposia*, page 101. Texas A&M University. Turbomachinery Laboratories, 2001. doi:10.21423/R1HM4N.

[15] J.H.Redmond and F.W.Bott. Development of cryogenic electric motors. *SAE Transactions*, 72 (753D):257–268, Sept. 1964. doi:10.4271/640023.

[16] T.Jasinski, W.D.Stacy, S.C.Honkonen, and H.Sixsmith. A generic pump/compressor design for circulation of cryogenic fluids. In *Advances in Cryogenic Engineering*, pages 991–997. Springer, 1986. doi:10.1007/978-1-4613-2213-9-111.

[17] J.W.Mark. Submersible fans and pumps for cryogenic fluids. In *Advances in Cryogenic Engineering*, volume 31, pages 999–1005. Springer, 1986. doi:10.1007/978-1-4613-2213-9-112.

[18] B.L.Norris. Control system for fermilab's low temperature upgrade. In *Proceedings Particle Accelerator Conference*, volume 4, pages 2152–2156, May 1995. doi:10.1109/PAC.1995.505484.

[19] K.A.Muller and J.G.Bednorz. The discovery of a class of high-temperature superconductors. *Science*, 237(4819):1133–1139, Sept. 1987. doi:10.1126/science.237.4819.1133.

[20] T.Song, A.Ninomiya, and T.Ishigohka. Experimental study on induction motor with superconducting secondary conductors. *IEEE Transactions on Applied Superconductivity*, 17(2):1611–1614, June 2007. doi:10.1109/TASC.2007.897834.

[21] S.Nategh. Thermal analysis and management of high-performance electrical machines,kth school of electrical engineering,PhD dissertation. 2013.

[22] J.Kolowrotkiewicz, M.Baranski, W.Szelag, and L.Dlugiewicz. Fe analysis of induction motor working in cryogenic temperature. *COMPEL International Journal of Computations and Mathematics in Electrical*, 26(4):952–964, Aug. 2007. doi:10.1108/03321640710756294.

[23] M.Baranski and W.Szelag. Finite element analysis of transient electromagnetic-thermal phenomena in a squirrel cage motor working at cryogenic temperature. In *IET 8th International Conference on Computation in Electromagnetics (CEM 2011)*, pages 1–2, 2011. doi:10.1049/cp.2011.0075.

[24] C.Ai, Y.Huang, and H.Wang. Coupled electromagnetic and thermal analysis of a 15kw cryogenic induction motor for submerged liquefied natural gas pumps. In *2020 23rd International Conference on Electrical Machines and Systems (ICEMS)*, pages 745–748, 2020. doi:10.23919/ICEMS50442.2020.9290937.

[25] H.M.Kim, K.W.Lee, D.G.Kim, J.H.Park, and G.S.Park. Design of cryogenic induction motor submerged in liquefied natural gas. *IEEE Transactions on Magnetics*, 54(3):1–4, 2018. doi:10.1109/TMAG.2017.2751099.

[26] V.B.Honsinger. Sizing equations for electrical machinery. *IEEE Transactions on Energy Conversion*, EC-2(1):116–121, 1987. doi:10.1109/TEC.1987.4765812.

[27] X.Lv, D.Sun, and L.Sun. Determination of iron loss coefficients of ferromagnetic materials used in cryogenic motors. In *2019 22nd International Conference on Electrical Machines and Systems (ICEMS)*, pages 1–5, 2019. doi:10.1109/ICEMS.2019.8922160.

[28] G. Bertotti. General properties of power losses in soft ferromagnetic materials. *IEEE Transactions on Magnetics*, 24(1):621–630, Jan 1988. doi:10.1109/20.43994.

[29] G. Brown, A.Kascak, B.T.Ebihara, D.Johnson, B.B.Choi, M.W.Siebert, and C.J.Buccieri. Nasa glenn research center program in high power density motors for aeropropulsion. 2005.

[30] R.Jansen, C.L.Bowman, A.L.Jankovsky, R.W.Dyson, and J.L.Felder. Overview of nasa electrified aircraft propulsion research for large subsonic transports. 2017.

[31] O. S. University. Electric motor demonstrator sets two world records in two hours after five years of work, 2019. URL `http://https://car.osu.edu/news/2019/11/electric-motor-demonstrator-sets-two-world-records-two-hours-after-five-years-work`.

[32] T. Britannica. cryogenics. `https://www.britannica.com/science/cryogenics`, 2017.

[33] C. Steinmetz and E. Berg. *Theory and Calculation of Alternating Current Phenomena*. Electrical World And Engineer, 1^{st} edition, 1897.

[34] F.R.Fickett. Electrical properties of materials and their measurement at low temperatures. United States Government Printing Office, march 1982.

[35] D. C. Giancoli. *Physics*. Prentice Hal, 1^{st} edition, 1995.

[36] H. J. Hucek, K. E. Wilkes, K. R. Hanby, and J. K. Thompson. *Handbook on Materials for Superconducting Machinery*. Metals and Ceramics Information Center, 1^{st} edition, 1977.

[37] X. Lv, D. Sun, and L. Sun. Determination of iron loss coefficients of ferromagnetic materials used in cryogenic motors. In *2019 22nd International Conference on Electrical Machines and Systems (ICEMS)*, pages 1–5, December 2019. doi:10.1109/ICEMS.2019.8922160.

[38] G. Bertotti. Space-time correlation properties of the magnetization process and eddy current losses: Theory. *Journal of Applied Physics*, 54(9):5293–5305, 1983. doi:10.1063/1.332705.

[39] G. Bertotti. Physical interpretation of eddy current losses in ferromagnetic materials, theoretical considerations. *Journal of Applied Physics*, 57(6):2118–2126, 1985. doi:10.1063/1.334404.

[40] M. Biasion, J. F. P. Fernandes, P. J. da Costa Branco, S. Vaschetto, A. Cavagnino, and A. Tenconi. A comparison of cryogenic-cooled and superconducting electrical machines. *IEEE*, 2021.

[41] P. Duthil. Material properties at low temperature. pages 77–95. CERN, Ja 2015.

[42] JFE. Electrical steel sheets. `https://https://https://www.jfe-steel.co.jp/en/products/electrical/catalog/f1e-001.pdf`.

[43] D. R. Lide. *Handbook of Chemistry and Physics*. CRC Press, 84^{th} edition, 2004.

[44] Emde. About current redistribution, 1922.

[45] I. Boldea and S. A. Nasar. *The Induction Machines Design Handbook*. CRC Press, 2^{nd} edition, 2010.

[46] J. Pyrhonen, T. Jokinen, and V. Hrabovcova. *Design of Rotating Electrical Machines*. John Wiley & Sons, Ltd, 1 edition, 2008.

[47] Technical specifications of skf standard and special greases for capped deep groove ball bearings. table 1. `https://www.skf.com/group/products/rolling-bearings/engineered-products/hybrid-bearings/temperature-limits`, 2021.

[48] Deep groove ball bearings 6201-2z. `https://www.skf.com/group/products/rolling-bearings/ball-bearings/deep-groove-ball-bearings/productid-6201-2Z`, 2021.

[49] *SKF High performance, high temperature bearing grease LGHP 2*. SKF, 2020.

[50] A. E. Fitzgerald, J. Charles Kingsley, and S. D. Umans. *Electric Machinery*. McGraw-Hill, 6^{th} edition, 2003.

[51] R. Hooke. Lectures de potentia restitutiva, or, of spring explaining the power of springing bodies. Royal Society, 1678.

[52] R. E. Schramm, A. F. Clark, and R. P. Reed. A compilation and evaluation of mechanical, thermal, and electrical properties of selected polymers. U.S. Department of Commerce, National Bureau of Standards, 1973.

[53] J. J. Gniewek and E. Ploge. Cryogenic behavior of selected magnetic materials. *JOURNAL OF RESEARCH of the National Bureau of Standards*, 69C(3), September 1965.